DELFT UNIVERSITY OF TECHNOLOGY
DEPARTMENT OF GEOSCIENCES AND ENGINEERING

Master Thesis in Applied Earth Sciences

Flow in Fractured Media: a Darcy-Stokes-Brinkman Modelling Approach

by

Gabriella Morito Mansur

Supervisor: Dr. Hadi Hajibeygi

13^{th} February, 2018

Flow in Fractured Media: a Darcy-Stokes-Brinkman Modelling approach

by

Gabriella Morito Mansur

to obtain the degree of Master of Science
at the Delft University of Technology,
to be defended publicly on Tuesday February 13, 2018 at 3:30 PM.

Thesis committee:

Dr. H. Hajibeygi,	Civil Engineering and Geosciences, TU Delft
Prof. Dr. W.R. Rossen,	Civil Engineering and Geosciences, TU Delft
Dr. Ir. M.I. Gerritsma,	Aerospace Engineering, TU Delft
Prof. Dr. J. Bruining,	Civil Engineering and Geosciences, TU Delft

TU Delft

Abstract

Coupling between porous media and free flow is widely present in many applications. In fractured reservoirs, fractures are often treated as parallel (smooth) plates, between which the flow is assumed to be steady state fully developed, with no-slip boundary condition. Under these assumptions, the Darcy law is employed inside fractures with permeability (K_f) as a quadratic function of aperture (a), i.e., $K_f = a^2/12$. Although this model is a rough simplification of real rock fractures, it is still widely used in subsurface flow modelling.

This study aims to investigate the validity range of the so-called local cubic law (LCL) by using a Darcy-Stokes-Brinkman model in which a unified formulation describes the Stokes flow in the free-flow sub-domain and Darcy flow in the porous sub-domain. Two simulation strategies are developed: a sequentially coupled approach, and a fully coupled approach. The non-linear velocity profiles inside the free flow require enough grid resolution to be captured. As such, the grid resolution sensitivity is presented. More importantly, the permeability contrast γ between the two media is found to be an important factor for the applicability of the LCL (Darcy-Darcy) approach. A threshold of $\gamma \approx 10^{-7}$ is found, below which the difference between the two modelling approaches is negligible, and above which the LCL model no longer provide reasonable results.

Let the beauty of what you love be what you do.
– Rumi

Acknowledgement

I would like to thank my supervisor Dr. Hadi Hajibeygi for the encouragement and trust he has always deposited in me. You saw in me a potential I doubted I had, and gave me confidence to pursue this challenging work.

I am also grateful to Murat Kilic, who, in one February afternoon at the Shell Brazil office, told me: let's apply today to a Master degree at the TU Delft. Thank you for always pushing me in the right direction and for embracing me like your own family.

To Elisa Troian, who has always helped me be the best version of myself.

To Rafael Moraes, for the deep and fruitful discussions we had, but mainly the shallow and fun ones.

To the amazing friends I have met at the TU Delft, in special Roberto Trujillo, Diego Sanchez, Christian Perdomo, Irene Platteeuw and Ibrahim Mikati. With you I shared some of my best memories in the past two years.

To Matteo Cusini, who fought this battle by my side. I don't know how I would have done this without your everyday help, our almost daily discussions, and brainstorming together until late hours. It is truly inspiring to see the passion you have for your work and your eagerness to help those around you. You amaze me everyday with your positive attitude, quick-wittedness and brightness.

To my father, who has always supported all my decisions; who could never say no to me, if it means putting a smile on my face.

I will always be grateful to have the most loving mother, who is also my best friend. To know what unconditional love means is rare. And you gave me this.

And finally to Gal, who continues to give meaning to my life. You are the proof love goes beyond life and death. Once again, I dedicate this achievement to you.

Contents

1 Introduction **1**
- 1.1 Motivation . . . 1
- 1.2 Modelling coupled free and porous media flow . . . 3
  - 1.2.1 Two-domain approaches . . . 3
  - 1.2.2 Single-domain approaches . . . 4
- 1.3 Parallel plate model and cubic law . . . 6
- 1.4 Objective of this study . . . 8
- 1.5 Methods . . . 8

2 Mathematical model **11**
- 2.1 Governing equations . . . 11
  - 2.1.1 Free flow region . . . 11
  - 2.1.2 Porous region . . . 11
- 2.2 Reformulated problem . . . 12
- 2.3 Boundary conditions . . . 14

3 Solution strategy **17**
- 3.1 Finite-Volume discretisation . . . 17
  - 3.1.1 Continuity equation . . . 19
  - 3.1.2 Pressure equation . . . 20
  - 3.1.3 Momentum balance equations . . . 25
  - 3.1.4 Implementation of boundary conditions . . . 28
- 3.2 Fully coupled approach . . . 32
- 3.3 Sequentially coupled approach . . . 33
  - 3.3.1 Convergence criteria . . . 34

4 Numerical results **35**
- 4.1 Stokes flow: code validation and consistency study . . . 35
  - 4.1.1 Choice of permeability in the free flow region . . . 36
  - 4.1.2 Consistency of the discretisation scheme . . . 37
- 4.2 Sequentially coupled vs. Fully coupled approach . . . 38

4.3 Stokes-Brinkman model vs Darcy-Darcy model 39
4.3.1 Sensitivity to permeability contrast 41
4.3.2 Sensitivity to resolution 46

5 Conclusion **51**

List of Figures

1.1 Examples of fractures at different scales 2
1.2 Example of boundary conditions between free flow and porous media 4
1.3 Different ansatzes to model and to couple the problems in the free flow region with porous media 5
1.4 Direct modelling or pore-scale approach where the solid is explicitly represented 6
1.5 Scheme of real rock fracture, with wall roughness and variable aperture 7
1.6 Velocity profile of a Poiseuille flow between parallel plates . . 7
1.7 Fracture/free flow domain represented by the parallel plate model 9
1.8 Problem setup 10

2.1 Scheme of boundary conditions on domain 16

3.1 Representation of pressure-centered grid 18
3.2 Velocity staggered grid in x direction 18
3.3 Velocity staggered grid in y direction 18
3.4 ABCD control volume for mass balance on cell i,j 19
3.5 ABCD control volume for pressure-centered grid 20
3.6 ABCD control volume for pressure-centered grid with the respective velocities 22
3.7 ABCD control volume for u_x velocity staggered grid 25
3.8 ABCD control volume for u_y velocity staggered grid 27

4.1 Pure free flow domain 35
4.2 Infinite norm of the error vs. permeability in free flow region . 36
4.3 Velocity profiles for pure free flow 37
4.4 Infinite norm of the error vs. grid cell size Δy 37
4.5 Pressure profiles 38

4.6 Velocity profiles for the sequentially and fully coupled approaches 39
4.7 Varying aperture setup 41
4.8 Normalized difference versus permeability ratio 42
4.9 Velocity profiles for varying apertures and fixed $\gamma = 10^{-2}$ . . . 43
4.10 Velocity profiles for varying apertures and fixed $\gamma = 10^{-4}$ . . . 44
4.11 Velocity profiles for varying apertures and fixed $\gamma = 10^{-8}$ . . . 45
4.12 Change of aperture h_f with constant N_y 46
4.13 Change of aperture h_f with constant N_{y_f} 46
4.14 Normalized difference versus permeability ratio 47
4.15 Velocity profiles for varying permeability contrasts, $h_f = 1/2$ and $N_{y_f} = 320$ 48
4.16 Velocity profiles for varying permeability contrasts, $h_f = 1/4$ and $N_{y_f} = 320$ 49
4.17 Velocity profiles for varying permeability contrasts, $h_f = 1/8$ and $N_{y_f} = 320$ 50

Chapter 1

Introduction

1.1 Motivation

Coupled flow between porous media and free flow regions are observed in numerous industrial, environmental and medical domains of interest: for example, in the modelling of transport of contaminants in coastal areas, river or basins; in bio-engineering applications, where blood oxygenators and hemodialysis devices are based on the transport of chemicals from the main blood stream in the arteries through a porous membrane (Discacciati and Quarteroni, 2009); flow through oil filters (Iliev and Laptev, 2004); flow between porous fiber tows (Ryol Hwang and Advani, 2010), etc.

Another example is the fluid flow in fractures. Naturally fractured geological formations, such as carbonate reservoirs, are estimated to hold more than 60% of the world's proven oil reserves and 40% of the world's gas reserves, and contain fractures that range from microscopic fissures to kilometer-wide collections (Ahmed et al., 2006). Figure 1.1 shows some examples of fractures at different scales (Guerriero et al., 2013).

Besides naturally fractured geological formations, most geothermal resources occur in rocks that lack fracture permeability and fluid circulation, creating the so-called enhanced geothermal systems concept (EGS), which aims to create permeability through hydraulic stimulation or fracturing in order to activate existing rock fractures or create new ones (Pruess, 2006).

Hydraulic fracturing is also widely accepted and applied to improve the gas recovery in unconventional reservoirs - which include those with very low permeability, complicated geological settings and in-situ stress field etc - e.g., shale gas, tight gas and coal seam gas (Li et al., 2015).

That said, fractures play a major role in flow and transport, as they create complex paths for fluid movement, impacting reservoir characterization and, ultimately, production performance and total recovery; Therefore, they need

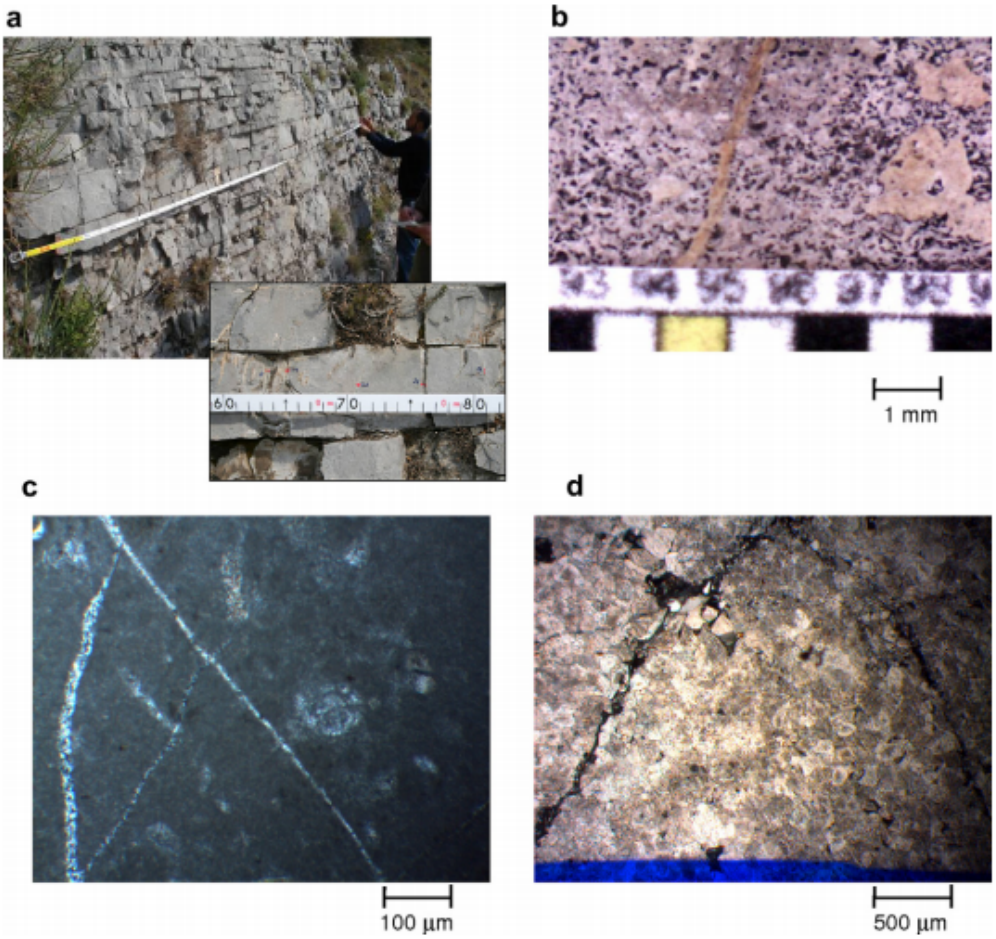

Figure 1.1: Examples of fractures at different scales

to be accounted for properly through adequate modelling.

One area of application of fluid flow modelling in fractures is the reservoir simulation of fractured petroleum reservoirs. The unexpected production behaviour of many fractured reservoirs emphasizes the need for better characterizing the fractures at various scales (Sarkar et al., 2004).

1.2 Modelling coupled free and porous media flow

Challenges in modelling flow in fractured reservoirs include (Iliev and Laptev, 2004)

- choice of an adequate mathematical model for the flow in each subregion
- Imposing proper interface conditions between the porous and fracture media
- efficient numerical method for field-scale simulations

All numerical algorithms for solving the coupled system of free fluid and porous media can be traditionally classified into two groups of methods: (1) two-domain and (2) single-domain approaches.

1.2.1 Two-domain approaches

The first group of methods uses different equations in different subdomains, e.g., the (Navier–)Stokes equation in the channel region and the Darcy/Brinkman model in the porous zones. These equations are coupled through suitable interface conditions, e.g., the well-known Beavers-Joseph empirical slip-flow condition, and that proposed by Le Bars and Worster, where the Stokes equation still applies down to a depth δ (fig. 1.2) (Le Bars and Worster, 2006).

The advantage of this approach is that one can use existing algorithms and software for solving (Navier–)Stokes equations and porous media flows. However, the disadvantage of the two–domain approach lies in coupling the conservation equations in both regions through the use of appropriate boundary conditions at the interface (Ehrhardt, 2000).

Figure 1.3 shows the different models used in free flow/porous media coupling problem.

Coupled (Navier-)Stokes/Darcy equations

This is the most common yet mathematically most difficult case, since Darcy and Navier-Stokes/Stokes equations are completely different systems of PDE and need different number of interface conditions (Iliev and Laptev, 2004).

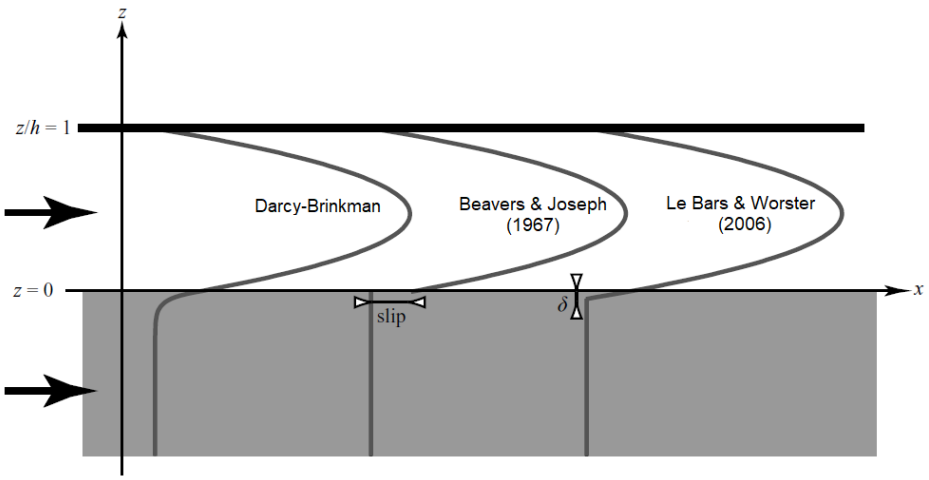

Figure 1.2: Example of boundary conditions between free flow and porous media

Coupled (Navier-)Stokes/Brinkman equations

In this case, the equations in the porous media (Brinkman) and in the channel region (Navier-Stokes/Stokes) are of the same type. The two most common types of coupling conditions that can be found in the literature are the continuity of velocity and continuity of the normal component of the stress tensor (Iliev and Laptev, 2004).

1.2.2 Single-domain approaches

The second group consists of those algorithms, which solely uses one system of equations in the whole domain (Navier–Stokes–Brinkman system) obtaining the transition between both fluid and porous regions through continuous spatial variations of properties (Ehrhardt, 2000).

The advantage of this approach is that it avoids the explicit formulation of boundary conditions at the fluid/porous interface, since velocity and stress continuity across the interface are readily satisfied.

Pore-scale modelling

In this approach, often referred to as direct numerical simulation (DNS) or pore-scale approach, the porous medium is represented as a connected

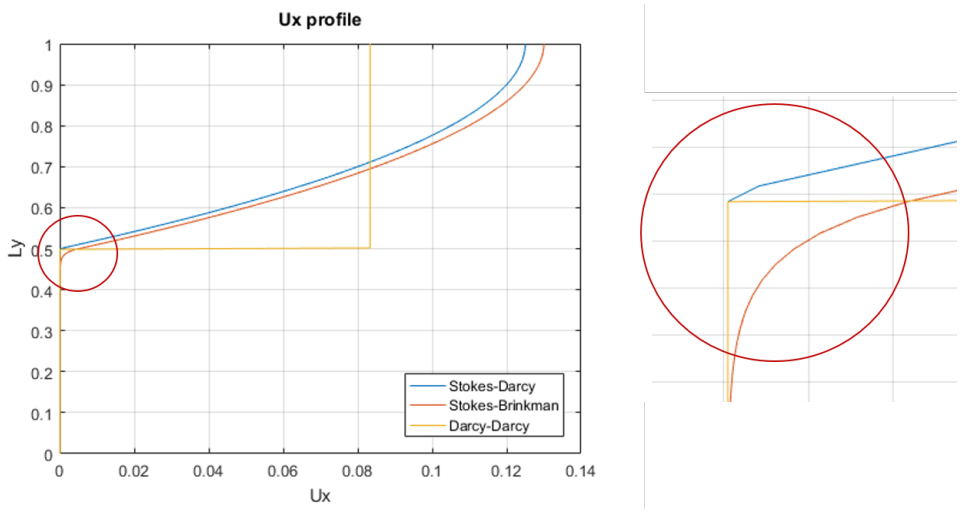

Figure 1.3: Different ansatzes to model and to couple the problems in the free flow region with porous media

domain of pore space filled with the fluid and the flow is governed by Navier-Stokes/Stokes equations, as illustrated in Fig. 1.4. There is no need for coupling conditions, since the same model is valid in the whole computational domain. Although this approach is physically correct and useful for theoretical purposes, it is not feasible for real-field porous media since it would need an unrealistic amount of CPU time and memory resources (Iliev and Laptev, 2004).

Darcy model

Darcy's law provides a linear relationship between pressure gradient and flow rate, where the fluid flow unknowns are averaged quantities. There is no macroscopic shear term associated with this equation, which, implemented all over the free flow/porous domain, has the profile depicted in Fig. 1.3.

Brinkman equation in the whole domain

This approach is a reformulation of the model described above, so that a single system of PDEs is governing the flow in the free flow and porous media domains. The coefficients vary such that it reduces to Stokes equations in the free flow region, and to Brinkman in the porous media (Iliev and Laptev,

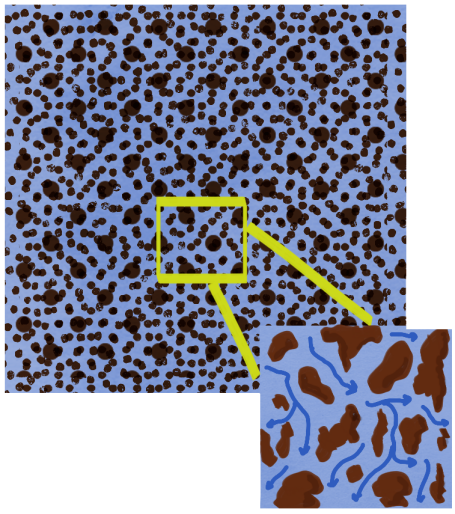

Figure 1.4: Direct modelling or pore-scale approach where the solid is explicitly represented

2004). This model is reviewed later in more detail.

1.3 Parallel plate model and cubic law

The simplest model of flow through a rock fracture is the so-called parallel plate model, in which the fracture is assumed to be bounded by two smooth plates with a constant distance from each other. This is the only geometrical model which allows an exact solution to be found, and it yields the so-called "cubic law" – which relates the hydraulic conductivity to the fracture aperture.

The main deviations from the cubic law comes from the fact that real rock fractures have rough walls, and, hence, have variable apertures (Fig. 1.5). Furthermore, there are usually regions where the two opposing faces of the fracture wall are in contact with each other, effectively reducing the aperture to zero and leading to the partial obstruction of the flow (Zimmerman and Bodvarsson, 1996).

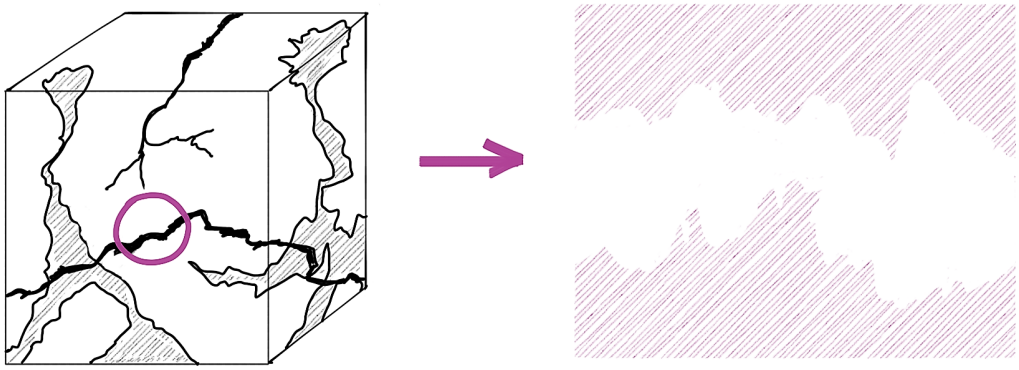

Figure 1.5: Scheme of real rock fracture, with wall roughness and variable aperture

For a Poiseuille flow between parallel plates (Fig. 1.6), which assumes an incompressible and Newtonian fluid, the average velocity in the x-direction reads (McKinley, 2013)

$$U_{avg} = -\frac{dP}{dx}\frac{H^2}{12\mu}, \tag{1.1}$$

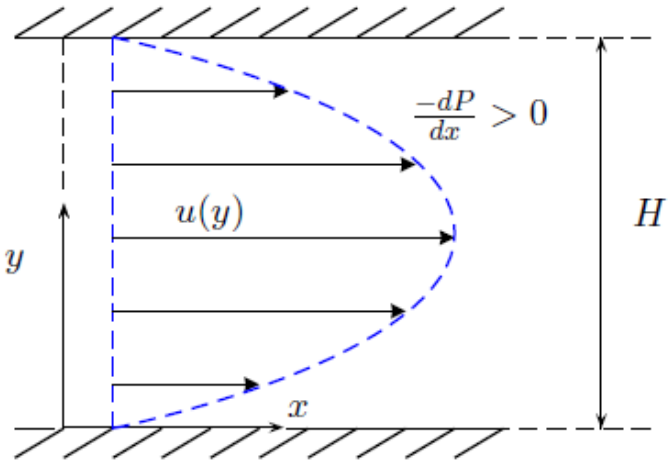

Figure 1.6: Velocity profile of a Poiseuille flow between parallel plates

The velocity profile $u(y)$ can be reconstructed through

$$u(y) = \left(\frac{H^2}{2\mu}\right)\left(-\frac{dP}{dx}\right)\left(\frac{y}{H}\left(1-\frac{y}{H}\right)\right), \tag{1.2}$$

When Eq. (1.1) is compared with the 1D Darcy velocity,

$$-\frac{dP}{dx}\frac{H^2}{12\mu} = -\frac{dP}{dx}\frac{k}{\mu}, \tag{1.3}$$

the permeability of a fracture can be identified as

$$k_f = \frac{H^2}{12}. \tag{1.4}$$

The cubic law relates the fracture transmissivity T_f to its aperture h_f, and reads (Zimmerman and Bodvarsson, 1996)

$$T_f = k_f A = \frac{w h_f^3}{12}, \tag{1.5}$$

where A is the cross-sectional area wh_f.

1.4 Objective of this study

Despite the assumption of an overly simplified fracture geometry, the parallel plate model is still widely used in subsurface flow modelling (Zimmerman and Bodvarsson, 1996). Hence, this study aims to verify the range of validity of the LCL, i.e., for which reservoir and flow conditions this model is reasonable – under a certain tolerance.

1.5 Methods

Since real reservoirs are large-scale, structurally complex and heterogeneous, it is reasonable to assume certain hypothesis as to obtain a simplified reservoir model, as shown in Fig.1.7. The fracture is represented by a channel bounded

by porous media regions which resembles the parallel plate model discussed in section 1.3.

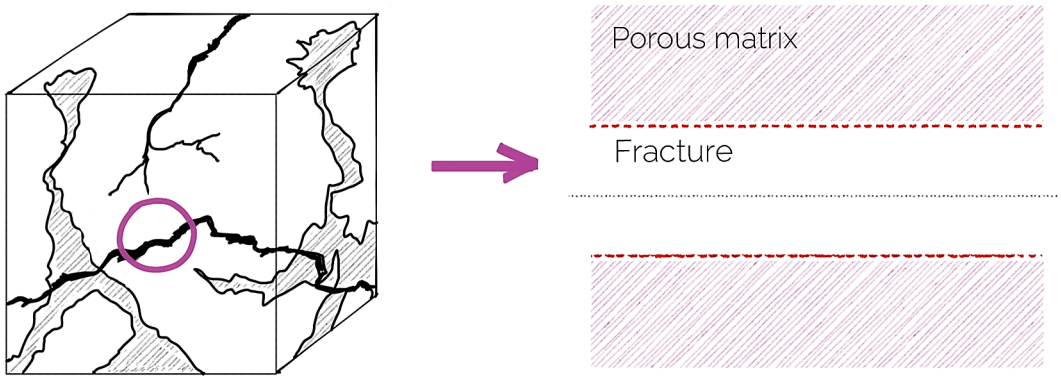

Figure 1.7: Fracture/free flow domain represented by the parallel plate model

The following assumptions are made:

1. Steady flow
2. Fully developed flow (no entrance effect, boundary layers are fully developed)
3. Incompressible flow ($\rho = constant$)
4. Newtonian fluid ($\mu = constant$)
5. Single phase flow
6. $\mu = \mu_{\text{eff}}$
7. Permeability $k = k(y)$, with binary values depending on free flow or porous flow regions
8. Viscous effects are dominant (Re $<<$ 1)
9. No flow or variation of properties in the z direction, with $u_z = 0$ and $\partial/\partial z = 0$ (2D flow)
10. Rectangular and symmetric control volume

The assumption of incompressibility is acceptable for liquids (e.g. water, gas-free oil) under typical subsurface conditions. The compressibility effect is important for transient problems, since it contributes to the storativity of the rock/fluid system. It is also reasonable to assume slow, laminar flow in most subsurface situations, which yields Re $<<$ 1, meaning inertial terms are negligible compared to viscous terms (Zimmerman and Bodvarsson, 1996).

Figure 1.8 illustrates the symmetrical half domain shown in Fig. 1.7, which has dimensions (L_x,L_y,1) and consists of two sub-domains:

- a **free flow** region with permeability k_{ff} and height corresponding to a variable half aperture h_f; and
- a **porous media** region with permeability k_{pm} and height $L_y - h_f$.

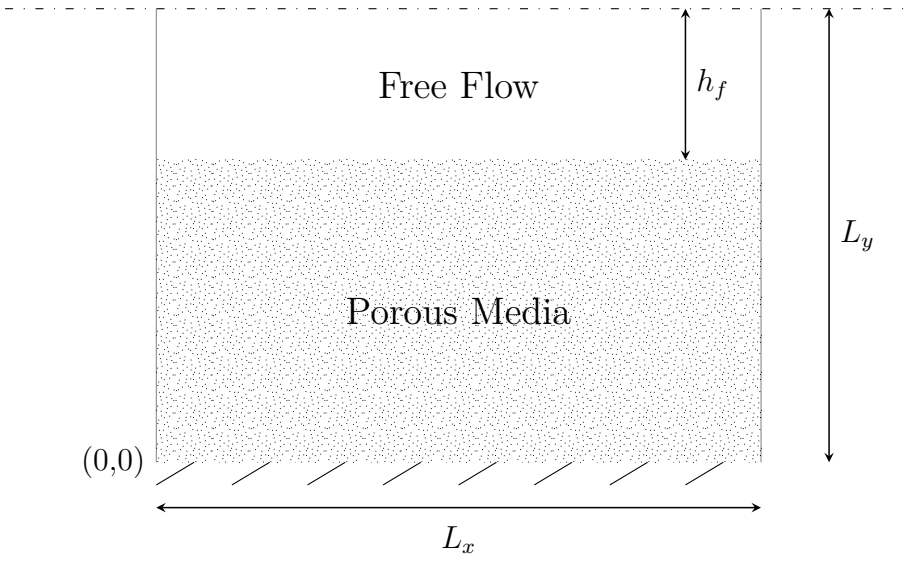

Figure 1.8: Problem setup

Chapter 2

Mathematical model

2.1 Governing equations

2.1.1 Free flow region

The flow in the free flow region is thus described by the incompressible Stokes "creeping flow" equations, which is a simplification of the Navier-Stokes equations for low fluid velocities, when the inertial forces are negligible compared to the viscous forces and the convective non-linear term $(u \cdot \nabla)u$ can be neglected. Together with the continuity equation derived from mass balance, they read

$$\begin{aligned} \mu \nabla^2 u &= \nabla p \\ \nabla \cdot u &= 0 \end{aligned} \tag{2.1}$$

2.1.2 Porous region

An incompressible flow in porous media is described by the Darcy model, which reads, for a source term equal zero,

$$\begin{aligned} u &= -\frac{k}{\mu} \nabla p \\ \nabla \cdot u &= 0 \end{aligned} \tag{2.2}$$

The Brinkman's extension of Darcy's law is mathematically and physically preferable to Darcy's law when examining boundary layer effects or to account for the high porosity of the porous media. By virtue of the macroscopic shear term it contains, the Brinkman formulation is fully compatible with the existence of boundary layer regions in the porous region (Neale and

Nader, 1974). Figure 1.3 illustrates how the Brinkman formulation, contrary to Darcy's, is able to capture and model boundary layer effects in the porous media.

$$\begin{aligned} -\mu_{\text{eff}}\nabla^2 u + \mu K^{-1} u + \nabla p = 0 \\ \nabla \cdot u = 0 \end{aligned} \tag{2.3}$$

Here, K is the permeability tensor, which reads, for a homogeneous isotropic medium,

$$K = \begin{bmatrix} k & 0 \\ 0 & k \end{bmatrix}$$

,

and μ_{eff} is the so-called effective viscosity of the fluid, which depends on the properties of the porous medium and can vary with relation to μ. Such effect is commonly attributed to tortuosity and porosity; it is, however, often and reasonably assumed that $\mu = \mu_{\text{eff}}$.

2.2 Reformulated problem

Having chosen the Brinkman model in the whole domain discussed in 1.2.2 and aiming to study the coupled fluid flow behaviour, one must solve three equations for three unknown variables: pressure and the two components of a 2D velocity field.

From the assumption that $\mu_{\text{eff}} = \mu$ and rearranging equation (2.3), pressure equation can be obtained by applying the divergence operator on the momentum balance,

$$\nabla \cdot \left[-k\nabla^2 u + u + \frac{k}{\mu}\nabla p \right] = 0,$$

$$\nabla \cdot (-k\nabla^2 u) + \underbrace{\nabla \cdot u}_{=0} + \nabla \cdot \left(\frac{k}{\mu}\nabla p \right) = 0.$$

From the continuity equation, $\nabla \cdot u = 0$. Rewriting, the pressure equation becomes, in vectorial and component form,

$$\nabla \cdot \left(-\frac{k}{\mu} \nabla p \right) = \nabla \cdot (-k \nabla^2 u), \tag{2.4a}$$

$$-\frac{\partial}{\partial x}\left(\frac{k}{\mu}\frac{\partial p}{\partial x}\right) - \frac{\partial}{\partial y}\left(\frac{k}{\mu}\frac{\partial p}{\partial y}\right) = -\frac{\partial}{\partial x}\left(k\frac{\partial^2 u_x}{\partial x^2} + k\frac{\partial^2 u_x}{\partial y^2}\right) - \frac{\partial}{\partial y}\left(k\frac{\partial^2 u_y}{\partial x^2} + k\frac{\partial^2 u_y}{\partial y^2}\right). \tag{2.4b}$$

The flow field is determined by the solution of the momentum balance equations in the x and y directions, that reads, in vectorial and component form,

$$-\mu \nabla^2 u + \frac{\mu}{k} u = -\nabla p, \tag{2.5a}$$

$$-\mu\left(\frac{\partial^2 u_x}{\partial x^2} + \frac{\partial^2 u_x}{\partial y^2}\right) + \frac{\mu}{k} u_x = -\frac{\partial p}{\partial x}, \tag{2.5b}$$

$$-\mu\left(\frac{\partial^2 u_y}{\partial x^2} + \frac{\partial^2 u_y}{\partial y^2}\right) + \frac{\mu}{k} u_y = -\frac{\partial p}{\partial y}. \tag{2.5c}$$

The single domain approach is formulated such that it perceives the different subdomains by varying the medium parameters, reducing the main Stokes-Brinkman equation to either Stokes-like model in the free flow region, or Darcy-like model in the porous media:

$$\underbrace{-\mu_{\text{eff}} \nabla^2 u}_{S} \overbrace{+\mu K^{-1} u}^{D} + \underbrace{\nabla p}_{S} = 0. \tag{2.6}$$

Defining the parameters α and β,

$$\underbrace{\alpha\nabla^2 u}_{S} + \overbrace{\beta u + \underbrace{\nabla p}_{S}}^{D} = 0. \tag{2.7}$$

When permeability $K >> 1$, the term β becomes negligible, and Eq. (2.7) assumes the Stokes form (Eq. (2.1)).

Otherwise, when permeability is $K << 1$, the term α becomes negligible close to α, and (2.7) assumes the Darcy's model form (Eq. (2.2)).

$$\begin{cases} \alpha \gg \beta, & \text{Stokes} \\ \alpha \ll \beta, & \text{Darcy} \end{cases} \tag{2.8}$$

2.3 Boundary conditions

The problem is governed by a set of second-order elliptic PDE's which thus requires boundary conditions over its entire boundary.

1. $\dfrac{dp}{dx} = \dfrac{pW - pE}{L_x} = 1$
2. $\dfrac{dp}{dx}(x = 0) = \dfrac{dp}{dx}(x = L_x)$
3. $u_y(y = 0, L_y) = 0$
4. $u_y(x = 0, L_x) = 0$
5. $\tau = \dfrac{\partial u_x}{\partial y}(y = 0, L_y) = 0$

At the axis of symmetry $y = L_y$, u_x reaches its maximum value and the viscous stress its minimum value, $\tau = \dfrac{\partial u_x}{\partial y} = 0$. The same condition is

applied at the south boundary, where the flow is Darcy-like and there are no shear terms.

At the north ($y = L_y$) and south ($y = 0$) domain's boundaries, the no-flow condition along the x-axis yields

$$u_y(y = 0, L_y) = 0 \qquad \Rightarrow \qquad \left.\frac{\partial u_y}{\partial x}\right|_{y=0,L_y} = 0 \qquad \Rightarrow \qquad \left.\frac{\partial^2 u_y}{\partial x^2}\right|_{y=0,L_y} = 0.$$

While the minimum stress condition yields

$$\left.\frac{\partial u_x}{\partial y}\right|_{y=0,L_y} = 0 \qquad \Rightarrow \qquad \left.\frac{\partial^2 u_x}{\partial x \partial y}\right|_{y=0,L_y} = 0 \qquad \Rightarrow_{Eq.(3.1)} \qquad \left.\frac{\partial^2 u_y}{\partial y^2}\right|_{y=0,L_y} = 0.$$

Substituting the above in Eq. (2.5c),

$$\left.\frac{\partial p}{\partial y}\right|_{y=0,L_y} = 0.$$

Which, for porous bottom face, is consistent with no-flow vertical (sealing) boundary condition.

At the west ($x = 0$) and east ($x = L_x$) domain's boundaries, where the velocity field only has its horizontal component $u = u_x$,

$$u_y(x = 0, L_x) = 0 \quad \Rightarrow \quad \left.\frac{\partial u_y}{\partial y}\right|_{x=0,L_x} = 0 \quad \Rightarrow \left.\frac{\partial^2 u_y}{\partial y^2}\right|_{x=0,L_x} = 0$$

$$\hookrightarrow_{Eq.(3.1)} \Rightarrow \left.\frac{\partial u_x}{\partial x}\right|_{x=0,L_x} = 0 \Rightarrow \left.\frac{\partial^2 u_x}{\partial x^2}\right|_{x=0,L_x} = 0$$

Applying $\partial/\partial x$ to Eq. (2.5b) and substituting the above,

$$-\mu\frac{\partial}{\partial x}\left(\frac{\partial^2 u_x}{\partial x^2}+\frac{\partial^2 u_x}{\partial y^2}\right)+\frac{\partial}{\partial x}\left(\frac{\mu}{k}u_x\right)=-\frac{\partial}{\partial x}\left(\frac{\partial p}{\partial x}\right),$$

$$-\mu\cancelto{0}{\frac{\partial^3 u_x}{\partial x^3}}-\mu\frac{\partial}{\partial y^2}\cancelto{0}{\left(\frac{\partial u_x}{\partial x}\right)}+\frac{\mu}{k}\cancelto{0}{\left(\frac{\partial u_x}{\partial x}\right)}=-\frac{\partial^2 p}{\partial x^2},$$

$$\left.\frac{\partial^2 p}{\partial x^2}\right|_{x=0,L_x}=0.$$

The above says that, as long as k = k(y), pressure gradient is constant on the west and east boundaries.

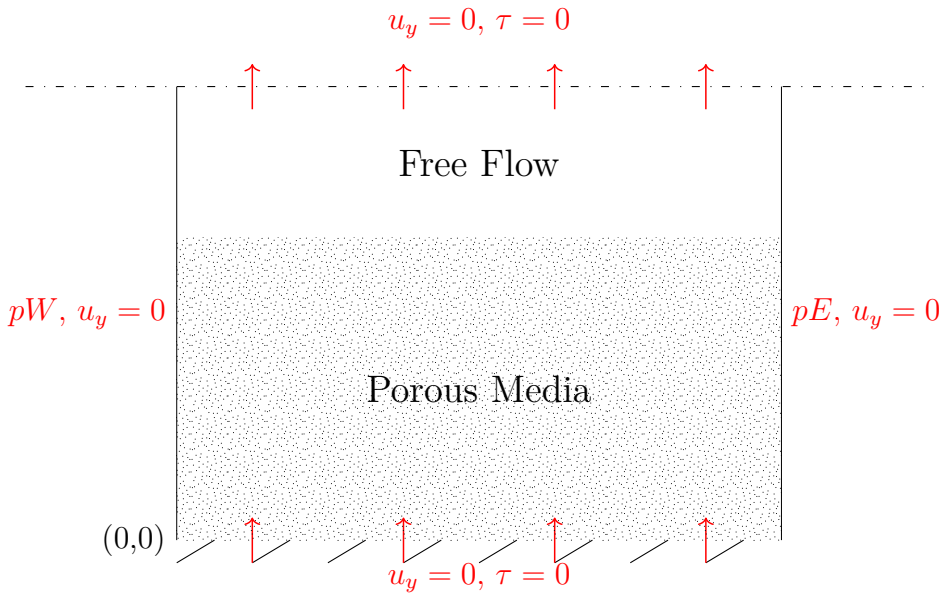

Figure 2.1: Scheme of boundary conditions on domain

Chapter 3

Solution strategy

3.1 Finite-Volume discretisation

The finite-volume discretisation scheme guarantees the conservation of relevant properties for each finite size cell, which makes this method attractive for engineering purposes.

The numerical algorithm consists of the following steps:

1. Integration of the governing equations of fluid flow over all the domain's control volumes and applying Gauss' divergence theorem
2. Discretisation of the governing equations into a system of algebraic equations
3. Solution of the algebraic equations by an iterative method

The domain represented in figure 1.8 is discretised into a (N_x, N_y) grid with finite control volumes, where $V = \Delta x \Delta y \Delta z$, and $\Delta z = 1$. The pressure grid (fig 3.1) is built such that pressure is cell-centered, and velocity is on the interfaces (3.1).

The velocity grid is built such that velocity is cell-centered, with the pressure nodes on the corners. This so-called staggered grid avoids unrealistic/non-physical behaviour from oscillating pressure fields, besides not requiring interpolations to calculate velocities, since they are exactly where they are required for scalar transport (Versteeg and Malalasekera, 2007).

Figures 3.2 and 3.3 depict the staggered grids for velocity in the x and y direction, respectively.

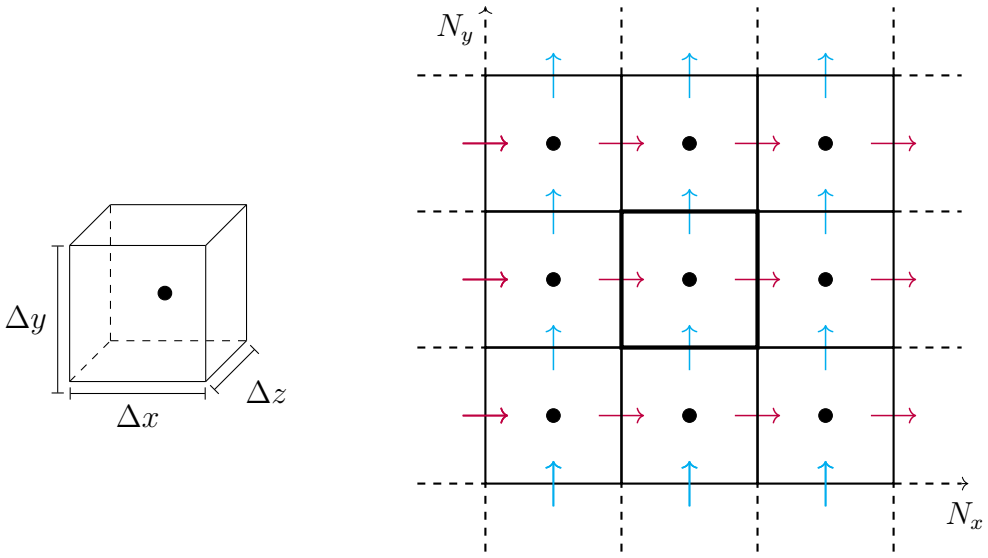

Figure 3.1: Representation of pressure-centered grid

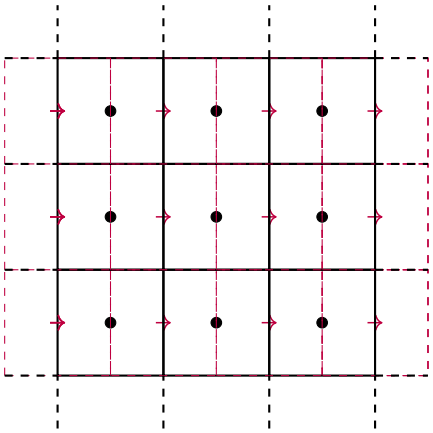

Figure 3.2: Velocity staggered grid in x direction

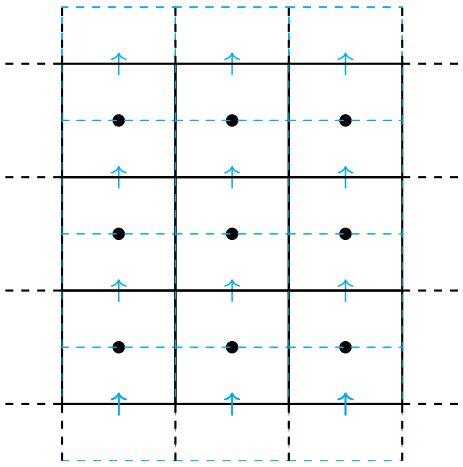

Figure 3.3: Velocity staggered grid in y direction

3.1.1 Continuity equation

Figure 3.4 represents the flux across control volume ABCD.

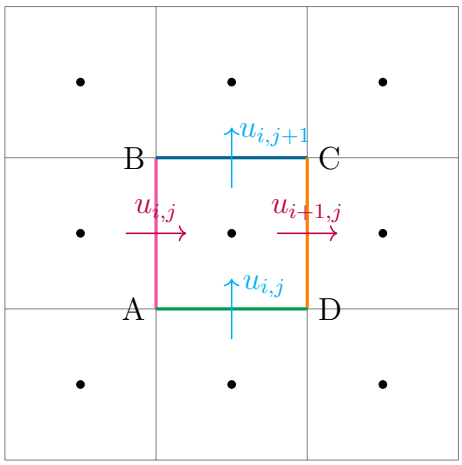

Figure 3.4: ABCD control volume for mass balance on cell i,j

The 2D continuity equation for an incompressible fluid derived from mass balance reads

$$\nabla \cdot u = \frac{\partial u_x}{\partial x} + \frac{\partial u_y}{\partial y} = 0. \tag{3.1}$$

Integrating and discretising Eq. (3.1) over the faces of ABCD,

$$\int_{AB} (u)n \approx -u^x_{i,j}|AB|, \tag{3.2a}$$

$$\int_{BC} (u)n \approx u^y_{i,j+1}|BC|, \tag{3.2b}$$

$$\int_{CD} (u)n \approx u^x_{i+1,j}|CD|, \tag{3.2c}$$

$$\int_{DA} (u)n \approx -u^y_{i,j}|DA|. \tag{3.2d}$$

Summing up the set of equations (3.2),

$$\Delta y(u^x_{i+1,j} - u^x_{i,j}) + \Delta x(u^y_{i,j+1} - u^y_{i,j}) = 0. \tag{3.3}$$

3.1.2 Pressure equation

The pressure equation described in Eq. (2.4a) is discretised in steps, beginning with its LHS. A mobility parameter $\lambda = k/\mu$ is defined, which is harmonically averaged on the cell interfaces.

Applying the divergence theorem results in

$$\int_V \nabla \cdot (-\lambda \nabla p) dv = \int_{\partial V} (-\lambda \nabla p) \cdot \overrightarrow{n}\, ds. \tag{3.4}$$

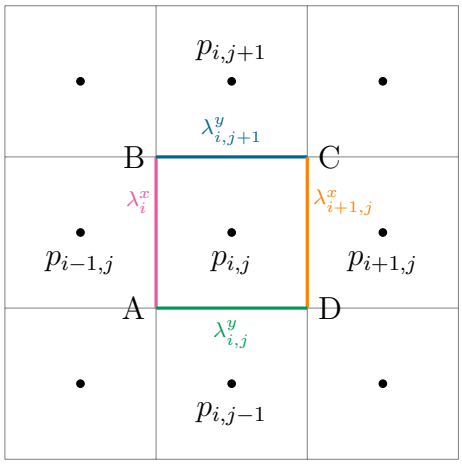

Figure 3.5: ABCD control volume for pressure-centered grid

Integrating and discretising Eq. (3.4) over the control cell ABCD shown in fig 3.5,

The integrals are approximated using discrete variables. The integral over the faces of ABCD and the volumetric integral gives

$$\int_{AB} (-\lambda \nabla p) n \approx \left[\lambda^x_{i,j} \frac{p_{i,j} - p_{i-1,j}}{\Delta x} \right] |AB|, \tag{3.5a}$$

$$\int_{BC} (-\lambda \nabla p) n \approx \left[\lambda^y_{i,j+1} \frac{p_{i,j} - p_{i,j+1}}{\Delta y} \right] |BC|, \tag{3.5b}$$

$$\int_{CD} (-\lambda \nabla p) n \approx \left[\lambda^x_{i+1,j} \frac{p_{i,j} - p_{i+1,j}}{\Delta x} \right] |CD|, \tag{3.5c}$$

$$\int_{DA} (-\lambda \nabla p) n \approx \left[\lambda^y_{i,j} \frac{p_{i,j} - p_{i,j-1}}{\Delta y} \right] |DA|. \tag{3.5d}$$

Summing up the set of equations (3.5),

$$\begin{aligned} &\underbrace{\frac{\lambda^x_{i,j}\Delta y}{\Delta x}}_{T^x_{i,j}}(p_{i,j} - p_{i-1,j}) + \underbrace{\frac{\lambda^x_{i+1,j}\Delta y}{\Delta x}}_{T^x_{i+1,j}}(p_{i,j} - p_{i+1,j}) + \\ &+ \underbrace{\frac{\lambda^y_{i,j}\Delta x}{\Delta y}}_{T^y_{i,j}}(p_{i,j} - p_{i,j-1}) + \underbrace{\frac{\lambda^y_{i,j+1}\Delta x}{\Delta y}}_{T^y_{i,j+1}}(p_{i,j} - p_{i,j+1}) = RHS. \end{aligned} \tag{3.6}$$

The transmissibility coefficient T, which contains mobility and dimension parameters, when multiplied by the pressure difference between grid blocks, yields flow rate.

Following the same procedure for the RHS of Eq. (2.4a),

$$\int_V \nabla \cdot (-k\nabla^2 u)dv = \int_{\partial V} (-k\nabla^2 u) \cdot \overrightarrow{n}\, ds, \tag{3.7}$$

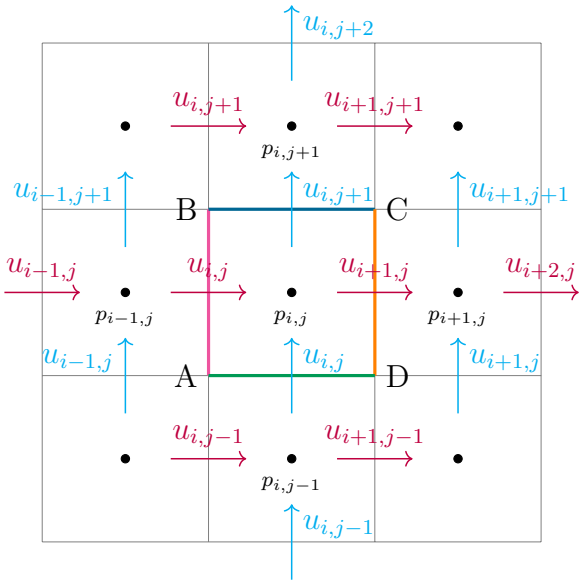

Figure 3.6: ABCD control volume for pressure-centered grid with the respective velocities

$$\int_{AB}(-k\nabla^2 u)n = k\left[\frac{\partial^2 u_x}{\partial x^2}+\frac{\partial^2 u_x}{\partial y^2}\right]_{AB}$$
$$\approx k^x_{i,j}\left[\frac{\frac{u^x_{i+1,j}-u^x_{i,j}}{\Delta x}-\frac{u^x_{i,j}-u^x_{i-1,j}}{\Delta x}}{\Delta x}+\frac{\frac{u^x_{i,j+1}-u^x_{i,j}}{\Delta y}-\frac{u^x_{i,j}-u^x_{i,j-1}}{\Delta y}}{\Delta y}\right]|AB|, \tag{3.8a}$$

$$\int_{BC}(-k\nabla^2 u)n = -k\left[\frac{\partial^2 u_y}{\partial x^2}+\frac{\partial^2 u_y}{\partial y^2}\right]_{BC}$$
$$\approx -k^y_{i,j+1}\left[\frac{\frac{u^y_{i+1,j+1}-u^y_{i,j+1}}{\Delta x}-\frac{u^y_{i,j+1}-u^y_{i-1,j+1}}{\Delta x}}{\Delta x}+\frac{\frac{u^y_{i,j+2}-u^y_{i,j+1}}{\Delta y}-\frac{u^y_{i,j+1}-u^y_{i,j}}{\Delta y}}{\Delta y}\right]|BC|, \tag{3.8b}$$

$$\int_{CD}(-k\nabla^2 u)n = -k\left[\frac{\partial^2 u_x}{\partial x^2}+\frac{\partial^2 u_x}{\partial y^2}\right]_{CD}$$
$$\approx -k^x_{i+1,j}\left[\frac{\frac{u^x_{i+2,j}-u^x_{i+1,j}}{\Delta x}-\frac{u^x_{i+1,j}-u^x_{i,j}}{\Delta x}}{\Delta x}+\frac{\frac{u^x_{i+1,j+1}-u^x_{i+1,j}}{\Delta y}-\frac{u^x_{i+1,j}-u^x_{i+1,j-1}}{\Delta y}}{\Delta y}\right]|CD|, \tag{3.8c}$$

$$\int_{DA}(-k\nabla^2 u)n = k\left[\frac{\partial^2 u_y}{\partial x^2}+\frac{\partial^2 u_y}{\partial y^2}\right]_{DA}$$
$$\approx k^y_{i,j}\left[\frac{\frac{u^y_{i+1,j}-u^y_{i,j}}{\Delta x}-\frac{u^y_{i,j}-u^y_{i-1,j}}{\Delta x}}{\Delta x}+\frac{\frac{u^y_{i,j+1}-u^y_{i,j}}{\Delta y}-\frac{u^y_{i,j}-u^y_{i,j-1}}{\Delta y}}{\Delta y}\right]|DA|. \tag{3.8d}$$

Finally, Eq. (3.9) is the discretised form of the pressure equation (Eq. (2.4a)), valid for a general cell (i, j) excluding the boundaries, which will be discussed later.

$$\begin{aligned}
T^x_{i,j}(p_{i,j} - p_{i-1,j}) + T^x_{i+1,j}(p_{i,j} - p_{i+1,j}) + T^y_{i,j}(p_{i,j} - p_{i,j-1}) + T^y_{i,j+1}(p_{i,j} - p_{i,j+1}) = \\
= k^x_{i,j}\Delta y \left[\frac{1}{\Delta x^2}(u^x_{i+1,j} - 2u^x_{i,j} + u^x_{i-1,j}) + \frac{1}{\Delta y^2}(u^x_{i,j+1} - 2u^x_{i,j} + u^x_{i,j-1})\right] + \\
-k^y_{i,j+1}\Delta x \left[\frac{1}{\Delta x^2}(u^y_{i-1,j+1} - 2u^y_{i,j+1} + u^y_{i+1,j+1}) + \frac{1}{\Delta y^2}(u^y_{i,j} - 2u^y_{i,j+1} + u^y_{i,j+2})\right] + \\
-k^x_{i+1,j}\Delta y \left[\frac{1}{\Delta x^2}(u^x_{i+2,j} - 2u^x_{i+1,j} + u^x_{i,j}) + \frac{1}{\Delta y^2}(u^x_{i+1,j+1} - 2u^x_{i+1,j} + u^x_{i+1,j-1})\right] + \\
+k^y_{i,j}\Delta x \left[\frac{1}{\Delta x^2}(u^y_{i+1,j} - 2u^y_{i,j} + u^y_{i-1,j}) + \frac{1}{\Delta y^2}(u^y_{i,j+1} - 2u^y_{i,j} + u^y_{i,j-1})\right]
\end{aligned} \tag{3.9}$$

A matrix A of transmissibilities is assembled, in order to solve the linear system for pressure $Ap = q$, i.e.

$$\underbrace{\begin{bmatrix}
\vdots & \vdots & \vdots & \vdots & \vdots & \vdots & \vdots & \vdots & \vdots \\
 & \vdots & \vdots & \vdots & \vdots & \vdots & \vdots & \vdots & \\
\cdots & -T^y_{i,j} & \cdots & -T^x_{i,j} & \sum T & -T^x_{i+1,j} & \cdots & -T^y_{i,j+1} & \cdots \\
 & \vdots & \vdots & \vdots & \vdots & \vdots & \vdots & \vdots & \\
\vdots & \vdots & \vdots & \vdots & \vdots & \vdots & \vdots & \vdots & \vdots
\end{bmatrix}}_{A}
\underbrace{\begin{bmatrix}
\vdots \\ p_{i,j-1} \\ \vdots \\ p_{i-1,j} \\ p_{i,j} \\ p_{i+1,j} \\ \vdots \\ p_{i,j+1} \\ \vdots
\end{bmatrix}}_{p}
= \begin{bmatrix} \\ \\ \\ \\ RHS \\ \\ \\ \\ \end{bmatrix}$$

The right-hand side (RHS) of the pressure equation is composed by the known velocities from the previous numerical iteration, and, at the boundary cells, also by the prescribed pressure gradient.

3.1.3 Momentum balance equations

The momentum balance equations (2.5b) and (2.5c) are discretised over the staggered velocity grids shown in figure (3.2) and (3.3).

Equation 2.5a is rearranged and an auxiliary vector ω is introduced,

$$-\nabla \cdot (\underbrace{\mu \nabla u - p\mathbf{e}}_{\omega}) + \frac{\mu}{k} u = 0, \tag{3.10}$$

where $\mathbf{e}$ is a unitary vector.

Equation (3.10) is then integrated over an assigned control volume ABCD in order to obtain a discretised equation for u_x and u_y.

$$-\int_{\partial ABCD} \omega n + \int_{ABCD} \frac{\mu}{k} u = 0 \tag{3.11}$$

Velocity in x-direction (u_x)

In this section, the subscript x is dropped for simplicity matters ($u_x = u$).

Resolving Eq. (3.11) over the ABCD control volume (fig 3.7) in order to obtain a discretised equation for a general velocity $u^x_{i,j}$:

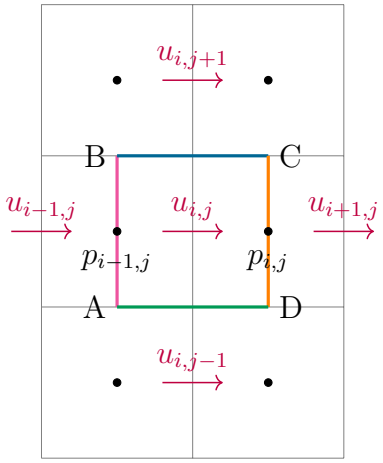

Figure 3.7: ABCD control volume for u_x velocity staggered grid

The integrals are approximated using discrete variables. The integral over the faces of ABCD and the volumetric integral gives us

$$\int_{AB} \omega n \approx \left[\mu \frac{u_{i,j} - u_{i-1,j}}{\Delta x} - p_{i-1,j}\right] |AB|, \tag{3.12a}$$

$$\int_{BC} \omega n \approx \left[\mu \frac{u_{i,j} - u_{i,j+1}}{\Delta y}\right] |BC|, \tag{3.12b}$$

$$\int_{CD} \omega n \approx \left[\mu \frac{u_{i,j} - u_{i+1,j}}{\Delta x} + p_{i,j}\right] |CD|, \tag{3.12c}$$

$$\int_{DA} \omega n \approx \left[\mu \frac{u_{i,j} - u_{i,j-1}}{\Delta y}\right] |DA|, \tag{3.12d}$$

$$\int_{ABCD} \frac{\mu}{k} u \approx u_{i,j} \frac{\Delta x \Delta y \Delta z}{\lambda^x_{i,j}}. \tag{3.12e}$$

Finally, summing up the interface and volumetric integrals, the discretised equation for the momentum balance in x-direction reads, for a general $u^x_{i,j}$,

$$\boldsymbol{-\mu a}\ u_{i,j-1}\ \boldsymbol{-\mu a^{-1}}\ u_{i-1,j}\ + [\boldsymbol{b\lambda^{-1} + 2\mu(a + a^{-1})}]\ u_{i,j}\ \boldsymbol{-\mu a^{-1}}\ u_{i+1,j}\ \boldsymbol{-\mu a}\ u_{i,j+1} = \Delta y\ p_{i-1,j} - \ \Delta y\ p_{i,j}. \tag{3.13}$$

Where $a = \Delta x/\Delta y$ and $b = \Delta x \Delta y \Delta z$.

Equation (3.13) is a linear system of the form $\boldsymbol{A^x} u_x = q_x$, where

$$A^x_{IJ} = \begin{cases} -\mu a, & J = I \pm (N_x + 1) \\ -\mu a^{-1}, & J = I \pm 1 \\ b\lambda^{-1} + 2\mu(a + a^{-1}), & J = I \end{cases} \tag{3.14}$$

Velocity in y-direction (u_y)

Once again, the subscript y is dropped for simplicity matters ($u_y = u$). Similarly, Eq. (3.11) is resolved for the ABCD control volume shown in fig 3.8 to obtain a discretised equation for $u^y_{i,j}$:

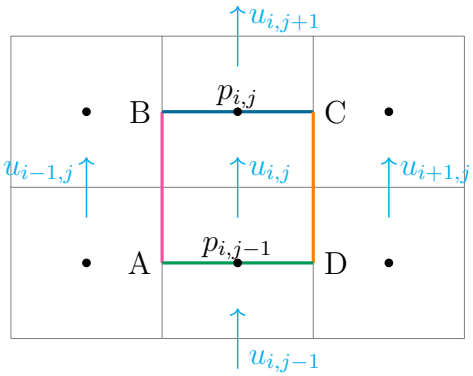

Figure 3.8: ABCD control volume for u_y velocity staggered grid

$$\int_{AB} \omega n \approx \left[\mu \frac{u_{i,j} - u_{i-1,j}}{\Delta x}\right] |AB|, \tag{3.15a}$$

$$\int_{BC} \omega n \approx \left[\mu \frac{u_{i,j} - u_{i,j+1}}{\Delta y} - p_{i,j}\right] |BC|, \tag{3.15b}$$

$$\int_{CD} \omega n \approx \left[\mu \frac{u_{i,j} - u_{i+1,j}}{\Delta x}\right] |CD|, \tag{3.15c}$$

$$\int_{DA} \omega n \approx \left[\mu \frac{u_{i,j} - u_{i,j-1}}{\Delta y} + p_{i,j-1}\right] |DA|, \tag{3.15d}$$

$$\int_{ABCD} \frac{\mu}{k} u \approx u_{i,j} \frac{\Delta x \Delta y \Delta z}{\lambda^y_{i,j}}. \tag{3.15e}$$

Summing up 3.15, the discretised equation for the momentum balance in x-direction reads, for a general $u^y_{i,j}$,

$$\boldsymbol{-\mu a}\ u_{i,j-1}\ \boldsymbol{-\mu a^{-1}}\ u_{i-1,j}\ + [\boldsymbol{b\lambda^{-1} + 2\mu(a + a^{-1})}]\ u_{i,j}\ \boldsymbol{-\mu a^{-1}}\ u_{i+1,j}\ \boldsymbol{-\mu a}\ u_{i,j+1} = \Delta x\ p_{i,j-1} - \ \Delta x\ p_{i,j}. \tag{3.16}$$

Equation (3.16) is a linear system of the form $\boldsymbol{A^y} u_y = q_y$, where

$$A^y_{IJ} = \begin{cases} -\mu a, & J = I \pm (N_y + 1) \\ -\mu a^{-1}, & J = I \pm 1 \\ b\lambda^{-1} + 2\mu(a + a^{-1}), & J = I \end{cases} \tag{3.17}$$

3.1.4 Implementation of boundary conditions

Equations (3.9), (3.13) and (3.16) describe the velocity and pressure fields for the overall domain. These equations are modified at domain's boundaries to incorporate the prescribed boundary conditions.

Pressure equation

At the west and east domain's boundaries pressure is prescribed. At the north and south boundaries, where no-flow condition is prescribed, the pressure gradients will be zero, i.e.,

$$\int_{BC,N} (-\lambda \nabla p) n \approx \left[\lambda^y_{i,j+1} \cancelto{0}{\frac{dp}{dy}}(y = L_y) \right] |BC|, \tag{3.18}$$

$$\int_{DA,S} (-\lambda \nabla p) n \approx \left[\lambda^x_{i,j} \cancelto{0}{\frac{dp}{dy}}(y = 0) \right] |DA|. \tag{3.19}$$

Momentum balance in x-direction

For the domain's west boundary ($i = 1$), half a control cell is used, with volume $V = (\Delta x/2)\Delta y \Delta z$. For these cells, the boundary conditions discussed in sec. 2.3 modify the volumetric and surface integrals on AB, BC and DA, with CD remaining the same:

$$\int_{AB,W} \omega n \approx \left[\mu \frac{\cancelto{0}{\partial u_x}}{\partial x} - p_W \right] |AB|, \tag{3.20a}$$

$$\int_{BC,W} \omega n \approx \left[\mu \frac{u_{i,j} - u_{i,j+1}}{\Delta y} \right] \frac{|BC|}{2}, \tag{3.20b}$$

$$\int_{CD,W} \omega n \approx \left[\mu \frac{u_{i,j} - u_{i+1,j}}{\Delta x} + p_{i,j} \right] |CD|, \tag{3.20c}$$

$$\int_{DA,W} \omega n \approx \left[\mu \frac{u_{i,j} - u_{i,j-1}}{\Delta y} \right] \frac{|DA|}{2}, \tag{3.20d}$$

$$\int_{ABCD,W} \frac{\mu}{k} u \approx u_{i,j} \frac{\Delta x \Delta y \Delta z}{2\lambda^x_{i,j}}. \tag{3.20e}$$

Summing up the set of eqs. (3.20), the discretised equation for the momentum balance in x-direction for $u_{1,j}$ reads

$$\boldsymbol{\frac{-\mu a}{2}}\ u_{i,j-1}\ + \left[\boldsymbol{\frac{b\lambda^{-1}}{2} + \mu(a + a^{-1})} \right]\ u_{i,j}\ \boldsymbol{-\mu a^{-1}}\ \ u_{i+1,j}\ \boldsymbol{\frac{-\mu a}{2}}\ u_{i,j+1} = \\ = \Delta y\ p_W - \ \Delta y\ p_{i,j}. \tag{3.21}$$

Likewise, for the east boundary ($i = N_x + 1$), the volumetric and surface

integrals on BC, CD and DA are modified, and AB remains the same:

$$\int_{AB,E} \omega n \approx \left[\mu \frac{u_{i,j} - u_{i-1,j}}{\Delta x} - p_{i-1,j}\right] |AB|, \tag{3.22a}$$

$$\int_{BC,E} \omega n \approx \left[\mu \frac{u_{i,j} - u_{i,j+1}}{\Delta y}\right] \frac{|BC|}{2}, \tag{3.22b}$$

$$\int_{CD,E} \omega n \approx \left[\mu \frac{\cancelto{0}{\partial u_x}}{\partial x} + p_E\right] |CD|, \tag{3.22c}$$

$$\int_{DA,E} \omega n \approx \left[\mu \frac{u_{i,j} - u_{i,j-1}}{\Delta y}\right] \frac{|DA|}{2}, \tag{3.22d}$$

$$\int_{ABCD,E} \frac{\mu}{k} u \approx u_{i,j} \frac{\Delta x \Delta y \Delta z}{2\lambda^x_{i,j}}. \tag{3.22e}$$

Summing up the set of equations (3.22), the discretised equation for the momentum balance in x-direction for $u_{N_x+1,j}$ reads

$$\boldsymbol{\frac{-\mu a}{2}}\ u_{i,j-1}\ \boldsymbol{-\mu a^{-1}}\ u_{i-1,j}\ + \left[\boldsymbol{\frac{b\lambda^{-1}}{2} + \mu(a + a^{-1})}\right]\ u_{i,j}\ \boldsymbol{\frac{-\mu a}{2}}\ u_{i,j+1} = \\ = \Delta y\ p_{i-1,j} - \ \Delta y\ p_E. \tag{3.23}$$

For the domain's north and south boundaries, the integrals over the BC and DA interfaces are respectively modified.

$$\int_{BC,N} \omega n \approx \cancelto{0}{\left[\mu \frac{\partial u_x}{\partial y}\right]} |BC| \tag{3.24}$$

$$\int_{DA,S} \omega n \approx \cancelto{0}{\left[\mu \frac{\partial u_x}{\partial y}\right]} |DA| \tag{3.25}$$

Momentum balance in y-direction

A Dirichlet boundary condition $u_y = 0$ is prescribed at all boundaries. There is, thus, no need to solve for u_y at the north and south boundaries. For the west and east boundaries, the integrals on faces AB and CD are respectively modified.

$$\int_{AB,W} \omega n \approx \left[\mu \frac{u_{i,j} - \cancelto{0}{u_y(x=0)}}{\Delta x/2}\right] |AB| \tag{3.26}$$

$$\int_{BC,E} \omega n \approx \left[\mu \frac{u_{i,j} - \cancelto{0}{u_y(x=L_x)}}{\Delta x/2}\right] |CD| \tag{3.27}$$

3.2 Fully coupled approach

The fully coupled approach solves both the momentum balance equations and the continuity equation simultaneously, dismissing the need for a pressure equation.

The set of equations (2.3) in for a 2D flow field reads

$$-\mu\left(\frac{\partial^2 u_x}{\partial x^2}+\frac{\partial^2 u_x}{\partial y^2}\right)+\frac{\mu}{k}u_x+\frac{\partial p}{\partial x}=0, \tag{3.28a}$$

$$-\mu\left(\frac{\partial^2 u_y}{\partial x^2}+\frac{\partial^2 u_y}{\partial y^2}\right)+\frac{\mu}{k}u_y+\frac{\partial p}{\partial y}=0, \tag{3.28b}$$

$$\frac{\partial u_x}{\partial x}+\frac{\partial u_y}{\partial y}=0. \tag{3.28c}$$

$$\underbrace{\begin{bmatrix} \begin{pmatrix} A_{u_x} \end{pmatrix} \begin{pmatrix} 0 \end{pmatrix} \begin{pmatrix} A_{p_x} \end{pmatrix} \\ \begin{pmatrix} 0 \end{pmatrix} \begin{pmatrix} A_{u_y} \end{pmatrix} \begin{pmatrix} A_{p_y} \end{pmatrix} \\ \begin{pmatrix} D_{u_x} \end{pmatrix} \begin{pmatrix} D_{u_y} \end{pmatrix} \begin{pmatrix} 0 \end{pmatrix} \end{bmatrix}}_{A} \underbrace{\begin{bmatrix} u_x \\ u_y \\ p \end{bmatrix}}_{X} = \begin{bmatrix} \\ RHS \\ \\ \end{bmatrix}$$

3.3 Sequentially coupled approach

The sequential coupling algorithm is essentially a guess-and-correct procedure which solves for the pressure and velocity fields sequentially in an iterative fashion.

The algorithm is initiated with a guessed velocity field $u^0 = u^*$ to solve Eq. (2.4), which yields a pressure field p'. The latter is then used to solve Eq. (2.5), yielding a new velocity field u'. If the solution has not yet converged, the loop restarts with an initial velocity field which corresponds to the solution of the previous iteration, $u^* = u'$. Likewise, the pressure field from the previous iteration is stored as $p^* = p'$.

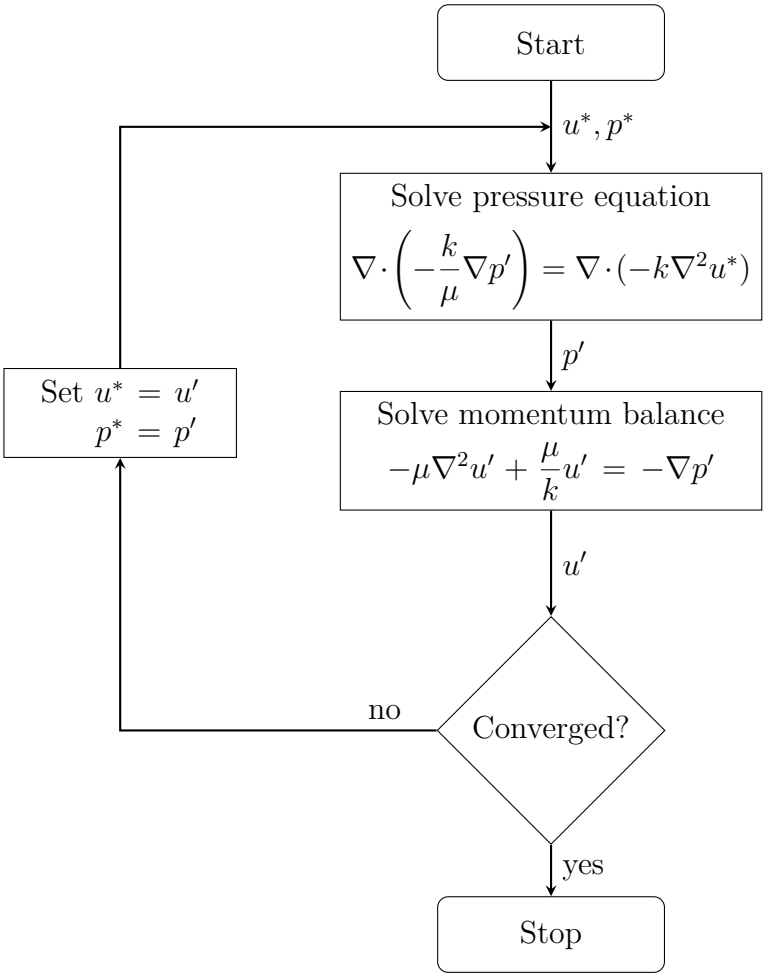

3.3.1 Convergence criteria

The criteria used to determine whether convergence has been achieved is based on residual values, which quantifies the local imbalance of a conserved variable in each control volume.

Recalling that the linear system for which the pressure is being solved is of the form $Ap = q$, The residual value at iteration ν for pressure is calculated as

$$R_p^\nu = q_u^\nu - Ap^\nu. \tag{3.29}$$

Likewise, the residual value for velocity is

$$R_u^\nu = q_u^\nu - A_u u^{\nu-1}. \tag{3.30}$$

At each iteration, eqs. (3.29) and (3.30) are calculated at each control cell, and convergence is achieved when the infinite norm of both residual vectors are smaller than a stipulated tolerance (Eq. (3.31)).

$$||R_p||_\infty < \text{tol} \quad \wedge \quad ||R_u||_\infty < \text{tol} \tag{3.31}$$

Chapter 4

Numerical results

Numerical results are presented in this chapter. First, the code is validated and consistency of the discretisation scheme is checked. This is done by simulating Stokes-Brinkman in pure free flow and comparing it against the analytical Stokes solution. Then, the sequentially coupled algorithm is compared against the fully coupled approach. Finally, the Stokes-Brinkman model results for different fracture apertures, permeability contrasts and grid sizes are presented. These results are then compared against the Darcy-Darcy model.

4.1 Stokes flow: code validation and consistency study

A 2D domain, as shown in Fig. 4.1, is considered. The whole domain is set to be a pure free flow region - i.e., no porous medium is present. Thus, the Stokes-Brinkman solution should coincide with the analytical solution to the Stokes equation. The simulation parameters are presented in table 4.1.

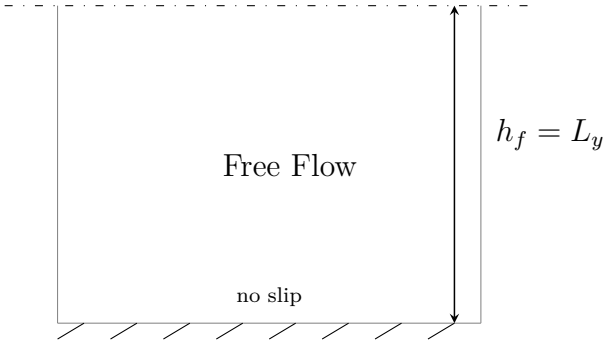

Figure 4.1: Pure free flow domain

Δp	L_x	L_y	h_f	N_x	N_y	k_{ff}
1	1	1	1	10	1280	$10^0 - 10^5$

Table 4.1: Parameters for pure Stokes flow

4.1.1 Choice of permeability in the free flow region

In this case, the permeability of the free flow region k_{ff} is varied. Figure 4.2 presents the infinite norm of the error of the Stokes-Brinkman solution with respect to the analytical Stokes solution, against k_{ff}, in a log-log scale.

Figure 4.3 illustrates two data points from the previous plot.

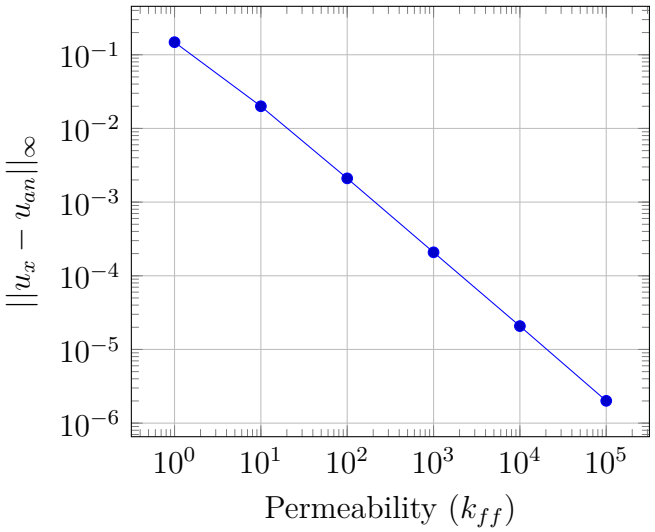

Figure 4.2: Infinite norm of the error vs. permeability in free flow region

Recalling Eq. (2.7), $\alpha >> \beta$ must hold so that the latter can become negligible for this equation to assume the Stokes form.

Figure 4.3a illustrates the case when the value of k_{ff} is not large enough and there is still influence of the term β.

Figure 4.3b shows the case where, using a larger k_{ff} value, the solution is much closer to the analytical solution, i.e., its behaviour is a better match for the expected Stokes solution.

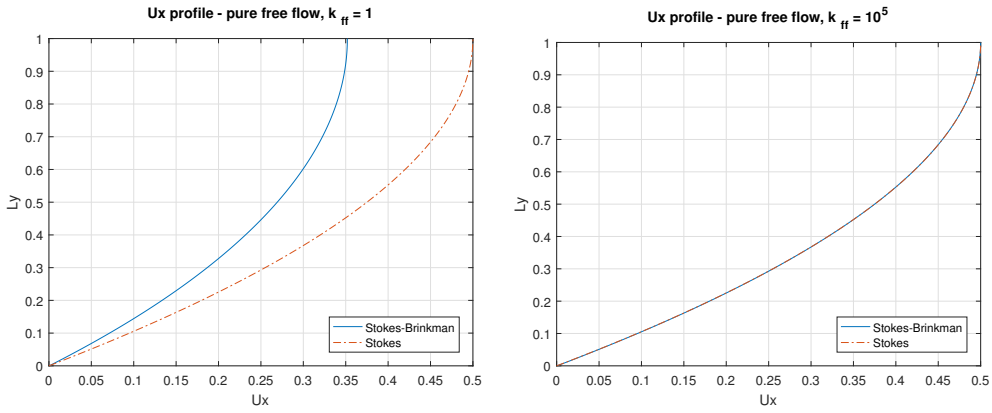

(a) $k_{ff} = 1$ (b) $k_{ff} = 10^5$

Figure 4.3: Velocity profiles for pure free flow

4.1.2 Consistency of the discretisation scheme

Since the exact solution to the Stokes problem is known, consistency can be checked. Figure 4.4 shows the log-log plot of the infinite norm of the error as a function of the grid cell size in the y direction, Δy. The system is found to be second order accurate, which is in accordance with the second order spatial discretisation scheme.

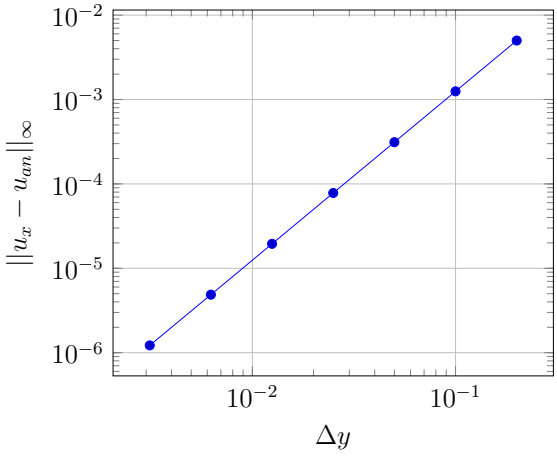

Figure 4.4: Infinite norm of the error vs. grid cell size Δy

4.2 Sequentially coupled vs. Fully coupled approach

In this section, the sequentially coupled algorithm presented in section 3.3 is verified against the fully coupled approach shown in section 3.2, which is taken as reference.

The pressure profiles obtained for the fully coupled and sequential coupling are shown on figs. 4.5a and 4.5b, respectively.

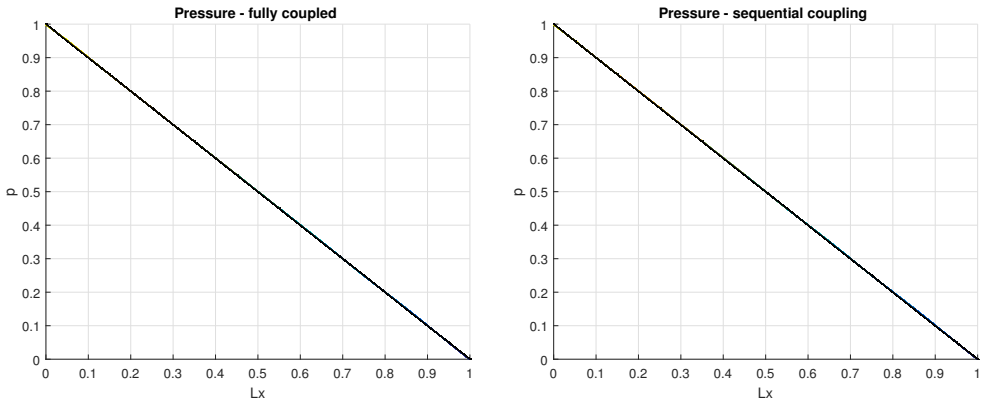

(a) Fully coupled (b) Sequential coupling

Figure 4.5: Pressure profiles

The results obtained through both approaches are in perfect agreement. In the sequential coupling, the solution converges after one iteration, as the initial guess for the velocity field $u^* = 0$ is correct. Recalling Eq. (2.4b),

$$LHS = -\frac{\partial}{\partial x}\left(\underbrace{k\frac{\partial^2 u_x}{\partial x^2}}_{[1]} + \underbrace{k\frac{\partial^2 u_x}{\partial y^2}}_{[2]}\right) - \frac{\partial}{\partial y}\left(\underbrace{k\frac{\partial^2 u_y}{\partial x^2}}_{[3]} + \underbrace{k\frac{\partial^2 u_y}{\partial y^2}}_{[4]}\right)$$

The constant pressure gradient yields $\dfrac{\partial u_x}{\partial x} = 0$ and $u_y = 0$, and permeability k = k(y) results in $\dfrac{\partial}{\partial x} = 0$. For this reason, the initial and final pressure profiles are the same.

On a hypothetical scenario where k = k(x) and the same sharp interface between free flow/porous media is kept, $\frac{\partial u_x}{\partial x} \neq 0$ and the final result would show an unrealistic peak on pressure. The same applies for the original k = k(y) but with an applied pressure gradient along the y-direction since this results in $u_y \neq 0$. Consequently, [4] would be non zero and the pressure gradient would no longer be constant.

Figure 4.6 presents the velocity profiles u_x for both coupling approaches, for different apertures and permeability contrasts.

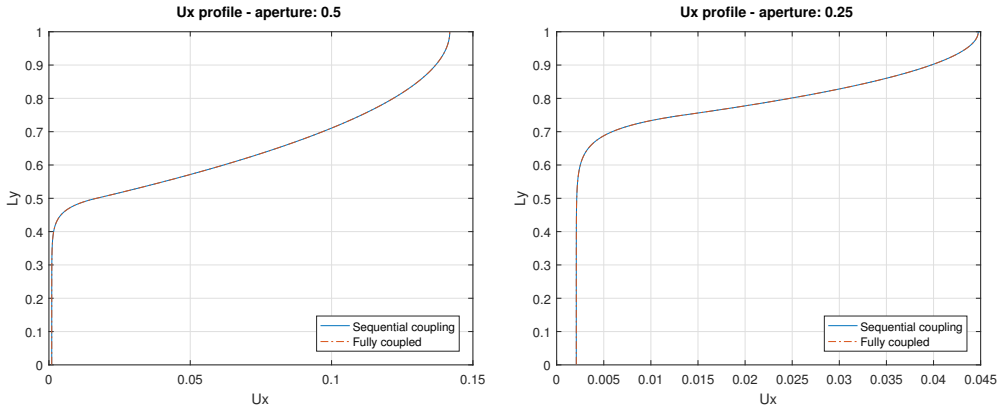

(a) $h_f = 1/2$, $k_{pm}/k_{ff} = 10^{-3}$ (b) $h_f = 1/4$, $k_{pm}/k_{ff} = 10^{-1}$

Figure 4.6: Velocity profiles for the sequentially and fully coupled approaches

4.3 Stokes-Brinkman model vs Darcy-Darcy model

The test cases present the sequential coupling results of velocity in x-direction (u_x), which is the solution to the discretised momentum balance presented in Eq. (3.13) with the respective boundary conditions.

The numerical solution, which corresponds to the Stokes-Brinkman approach, is compared against the analytical Darcy-Darcy approach, where flow in both free flow and porous media is governed by Darcy's law (Eq. (2.2)).

Permeability in the free flow is geometrically related to aperture as described in Eq. (1.4), and permeability in the porous media is the result of an applied contrast γ, where $k_{pm} = \gamma k_f$

Ultimately, the Darcy-Darcy approach is to be compared with the Stokes-Brinkman simulated velocity profile and verify, under a stipulated tolerance, the range of validity of Eq. (1.5).

This comparison is done in two manners:

1. qualitatively, through the comparison between the Stokes-Brinkman computed velocity profile and the reconstructed velocity profile plotted from Eq. (1.2), corresponding to the Darcy-Darcy approach, and observing how the two curves fit;

2. quantitatively, by calculating the normalized difference ϵ, between the averaged Stokes-Brinkman velocity profile U_x and the Darcy-Darcy velocity u_{x_D} in the whole domain.

$$U_x = \int_0^{L_y} u_x(y)dy$$

$$\epsilon = \frac{|u_{x_D} - U_x|}{u_{x_D}} \tag{4.1}$$

Table 4.2 shows the parameters used for the simulations.

Δp	L_x	L_y	N_x	k_{ff}
1	1	1	10	10^5

Table 4.2: Fixed parameters

Since $k = k(y)$, i.e., the value of permeability is constant along the x direction, a high resolution in the x direction is not necessary, thus, N_x is kept to a low, constant value.

Fracture aperture is equal to the factor h_f multiplied by the domain's length in the y direction L_y, but for simplicity matters, since $L_y = 1$, the fracture aperture is referred simply as h_f.

The assigned permeability of free flow, k_{ff}, is set to a value high enough to represent an infinitely permeable porous media, so that it mimics a free flow region.

4.3.1 Sensitivity to permeability contrast

The permeability ratio $\gamma = k_{pm}/k_f = 12k_{pm}/h_f^2$ is varied for different aperture sizes, as shown in Fig. 4.7. The remaining parameters are fixed according to table 4.2, and $Ny = 1280$.

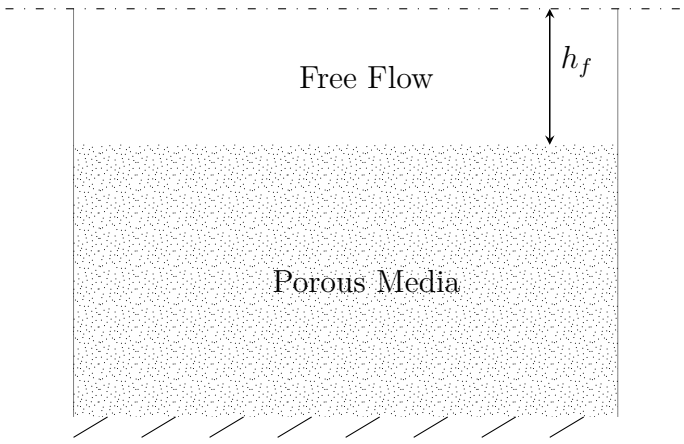

Figure 4.7: Varying aperture setup

Figure 4.8 shows the relationship between the normalized difference and permeability ratio. For each curve representing an aperture size, each value of γ corresponds to a different value of k_{pm}. Thus, an increasing contrast implies the same free flow permeability, but lower matrix permeability.

Figure 4.8 shows that there is a threshold of $\gamma \approx 10^{-7}$ below which the difference between the Stokes-Brinkman and Darcy-Darcy solutions is negligible.

Figures 4.9 - 4.11 show the influence of permeability contrast for varying apertures $h_f = 1/2$, $h_f = 1/4$ and $h_f = 1/8$.

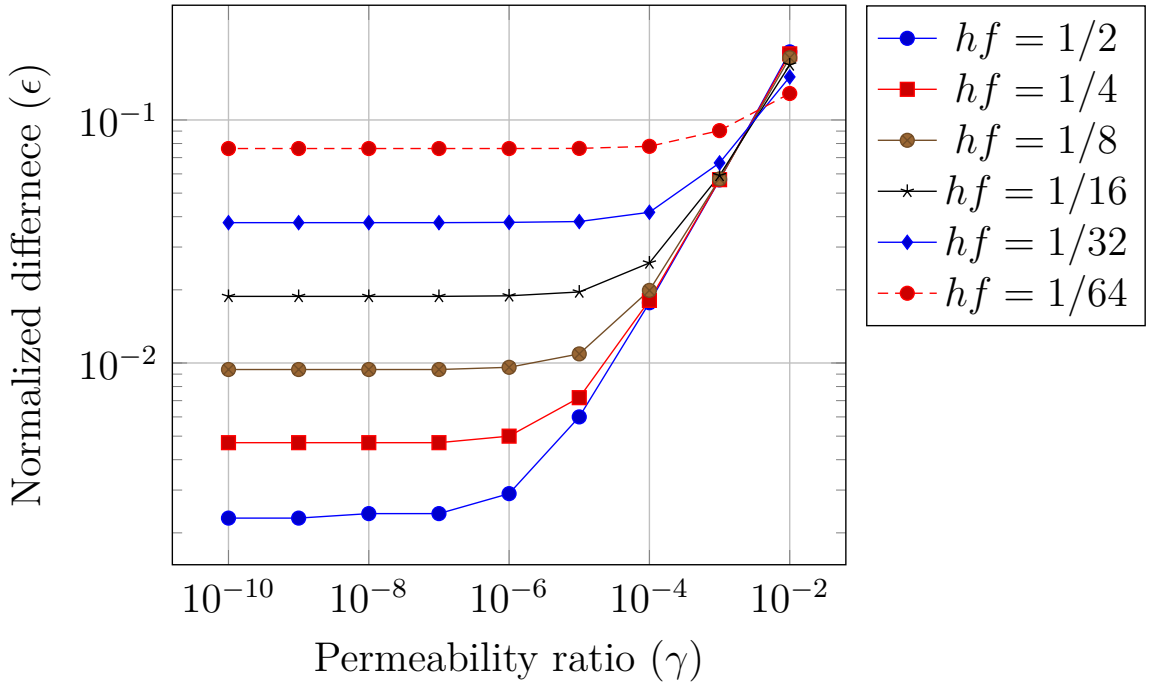

Figure 4.8: Normalized difference versus permeability ratio

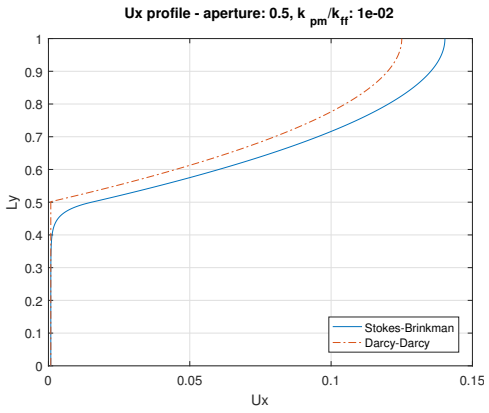

(a) $h_f = 1/2$

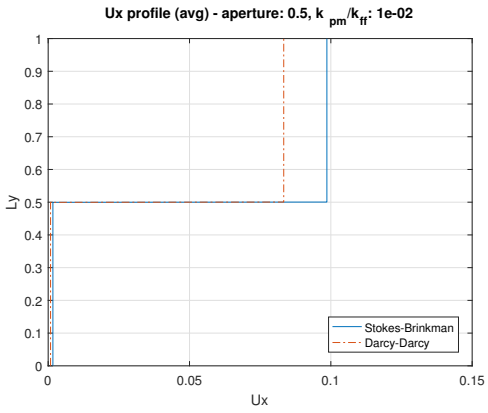

(b) $h_f = 1/2$

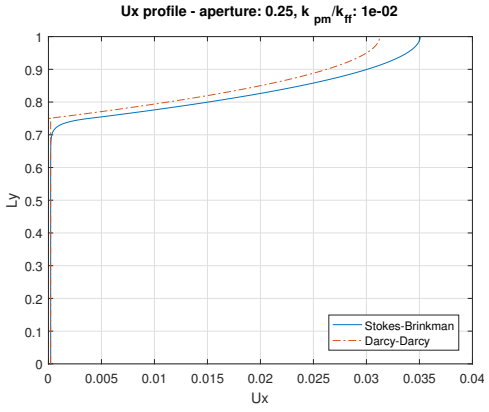

(c) $h_f = 1/4$

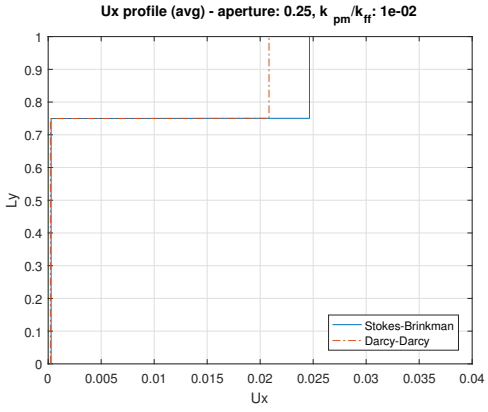

(d) $h_f = 1/4$

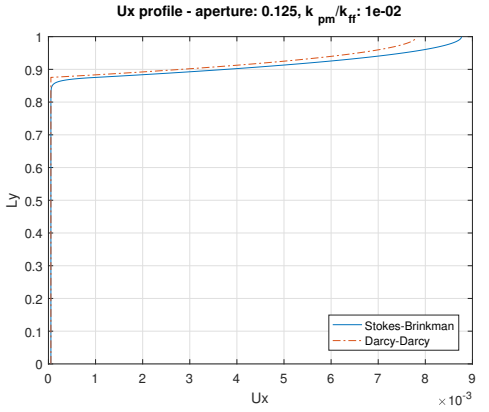

(e) $h_f = 1/8$

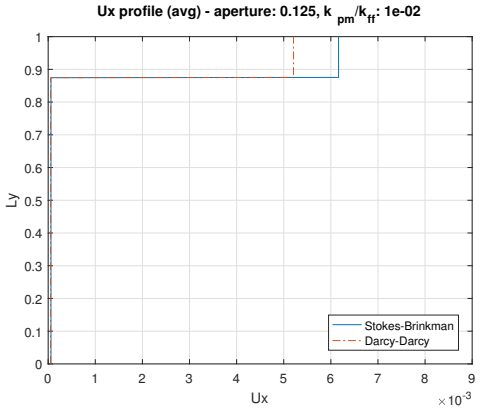

(f) $h_f = 1/8$

Figure 4.9: Velocity profiles for varying apertures and fixed $\gamma = 10^{-2}$

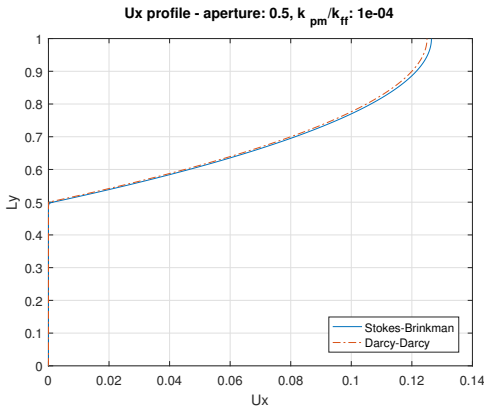

(a) $h_f = 1/2$

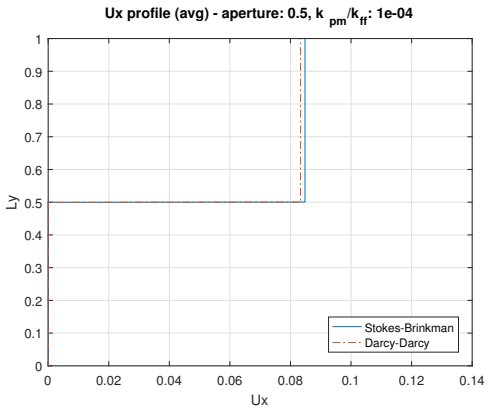

(b) $h_f = 1/2$

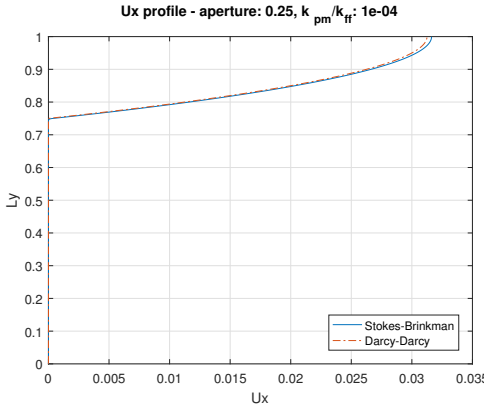

(c) $h_f = 1/4$

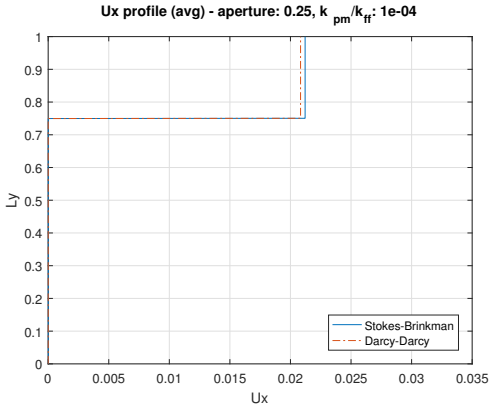

(d) $h_f = 1/4$

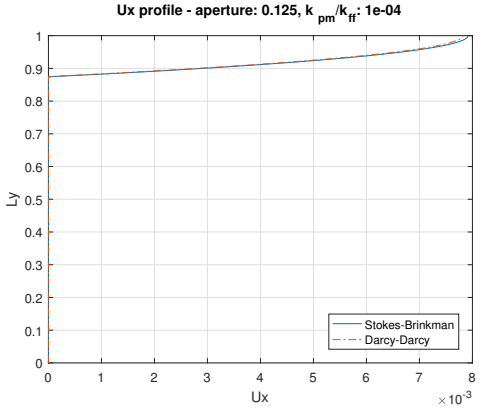

(e) $h_f = 1/8$

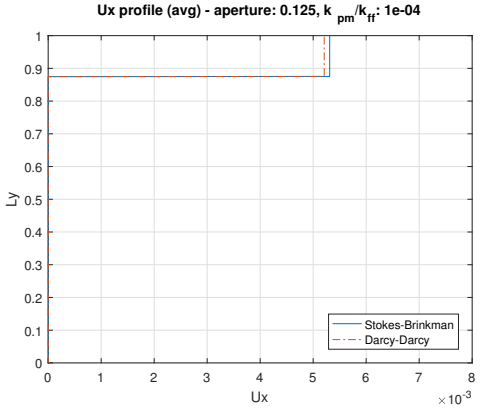

(f) $h_f = 1/8$

Figure 4.10: Velocity profiles for varying apertures and fixed $\gamma = 10^{-4}$

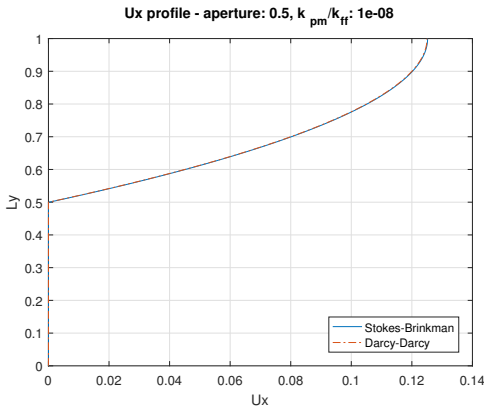

(a) $h_f = 1/2$

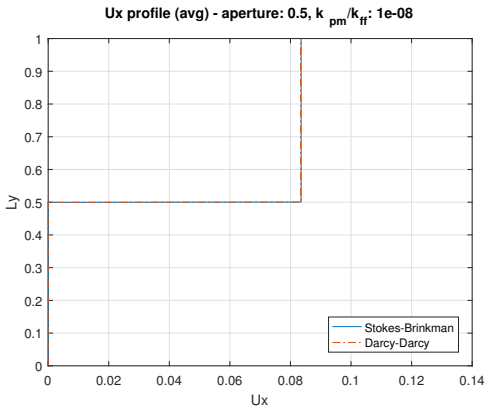

(b) $h_f = 1/2$

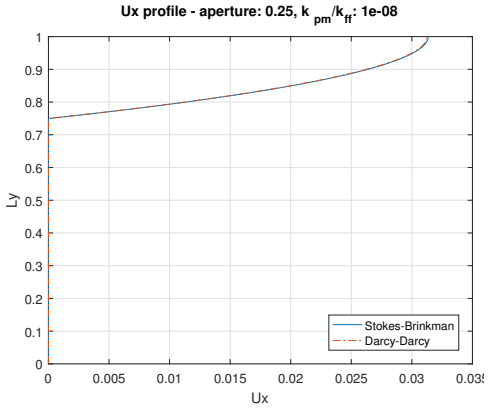

(c) $h_f = 1/4$

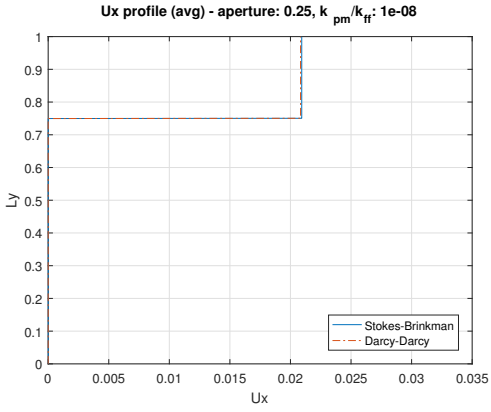

(d) $h_f = 1/4$

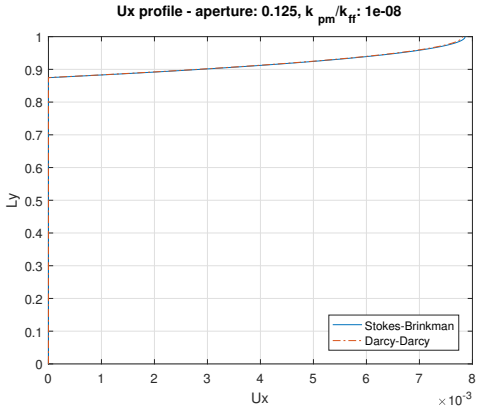

(e) $h_f = 1/8$

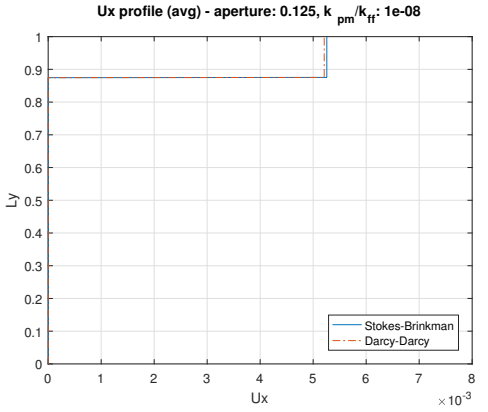

(f) $h_f = 1/8$

Figure 4.11: Velocity profiles for varying apertures and fixed $\gamma = 10^{-8}$

4.3.2 Sensitivity to resolution

The number of grid cells in the free flow region (N_{y_f}) decreases for a decreasing aperture size, as represented in Fig. 4.12. Thus, for a fixed resolution N_y, as aperture decreases, the normalized difference increases as an impact of loss of resolution.

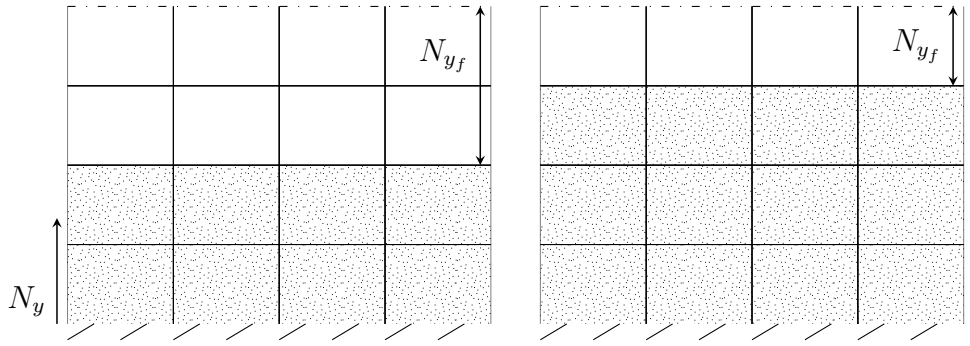

(a) $Ny = 4$, $h_f = 0.5$, $N_{y_f} = 2$ (b) $Ny = 4$, $h_f = 0.25$, $N_{y_f} = 1$

Figure 4.12: Change of aperture h_f with constant N_y

For a fixed resolution N_{y_f} in the fracture, the aperture and total resolution N_y varies such that $N_{y_f} = N_y h_f = \textit{constant}$, as represented by Fig. 4.13.

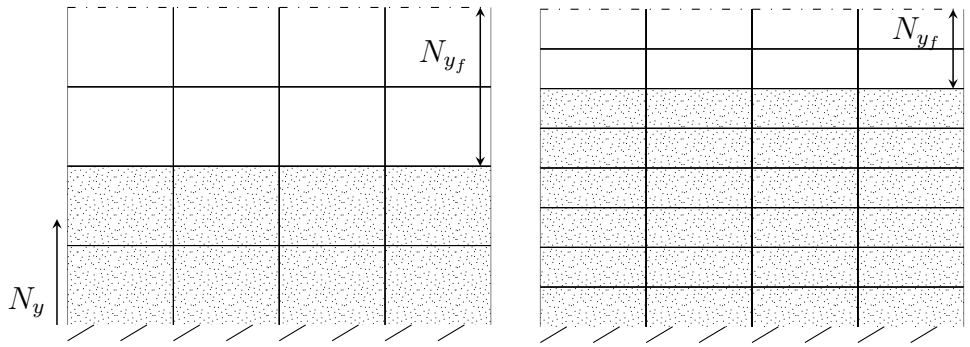

(a) $Ny = 4$, $h_f = 0.5$, $N_{y_f} = 2$ (b) $Ny = 8$, $h_f = 0.25$, $N_{y_f} = 2$

Figure 4.13: Change of aperture h_f with constant N_{y_f}

Figure 4.14 shows that as long as the resolution N_{y_f} is kept fixed, the normalized difference is the same for any fracture aperture.

Figures 4.15 - 4.17 show the influence of permeability contrast for fixed apertures $h_f = 1/2$, $h_f = 1/4$ and $h_f = 1/8$, for $N_{y_f} = N_y h_f = 320$.

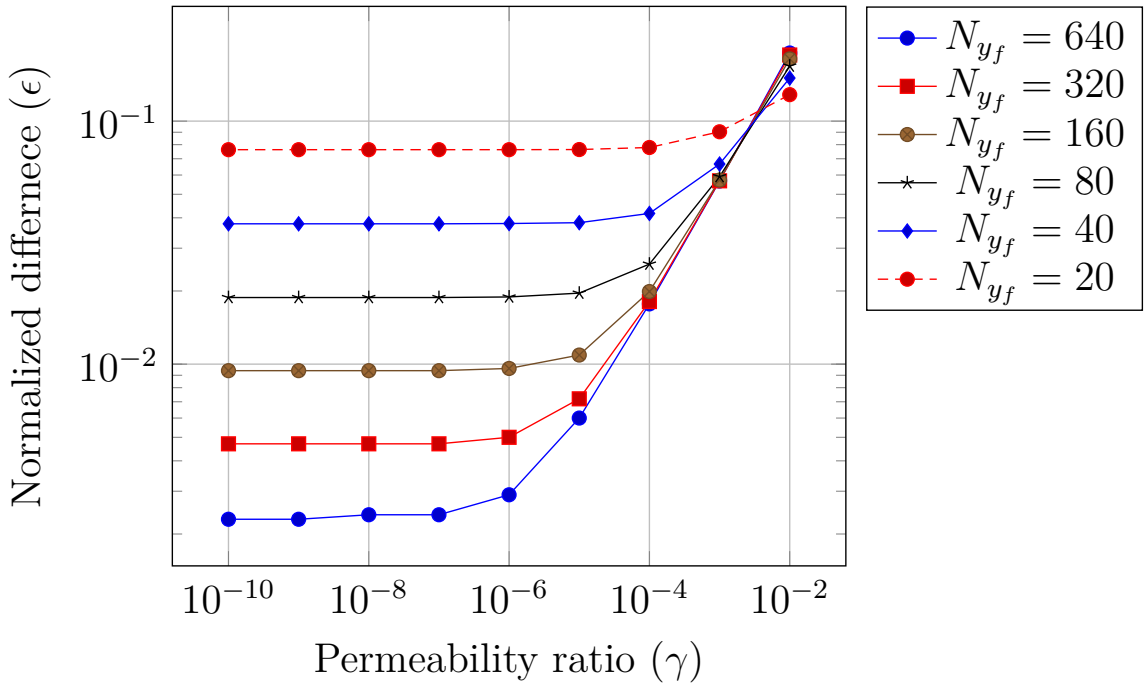

Figure 4.14: Normalized difference versus permeability ratio

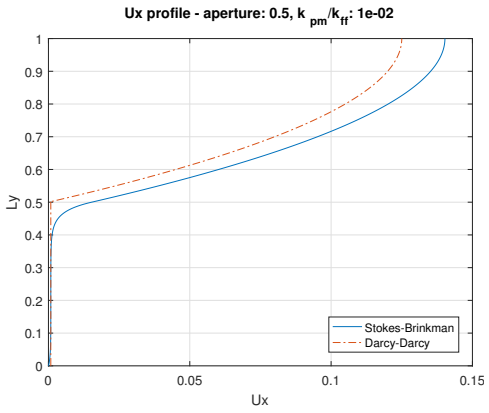

(a) $\gamma = 10^{-2}$

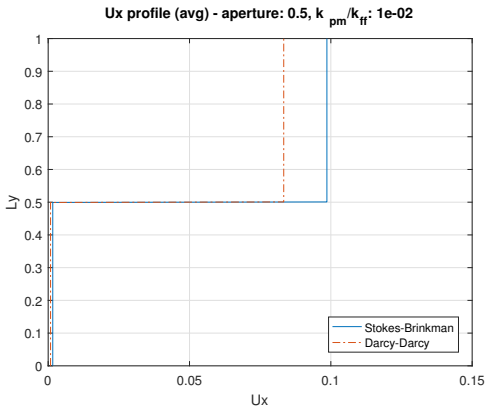

(b) $\gamma = 10^{-2}$

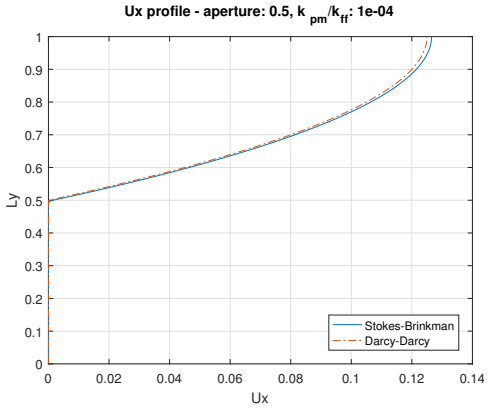

(c) $\gamma = 10^{-4}$

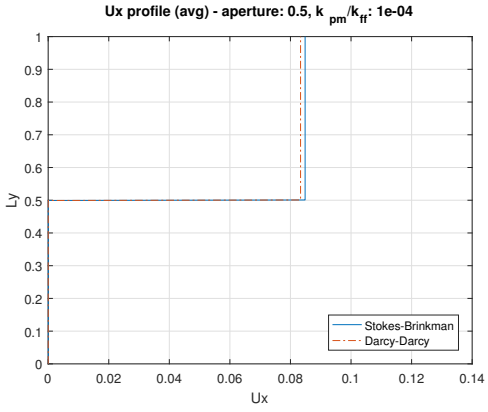

(d) $\gamma = 10^{-4}$

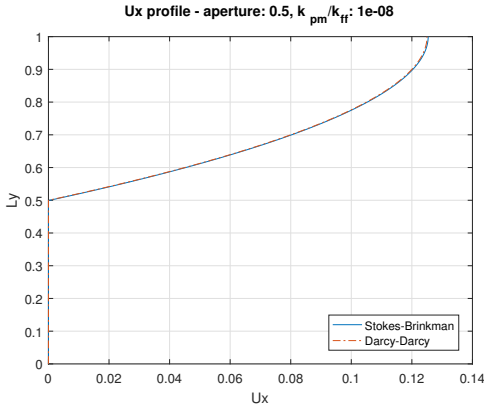

(e) $\gamma = 10^{-8}$

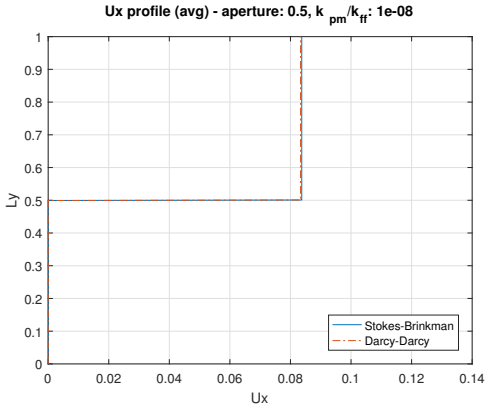

(f) $\gamma = 10^{-8}$

Figure 4.15: Velocity profiles for varying permeability contrasts, $h_f = 1/2$ and $N_{y_f} = 320$

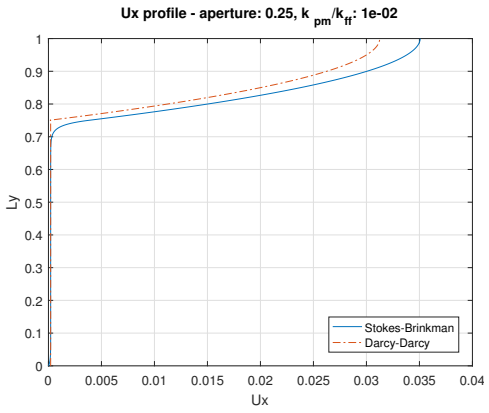

(a) $\gamma = 10^{-2}$

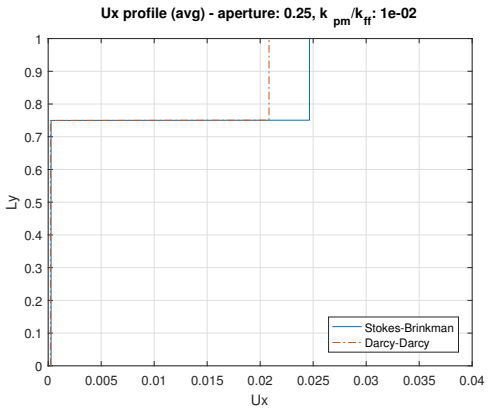

(b) $\gamma = 10^{-2}$

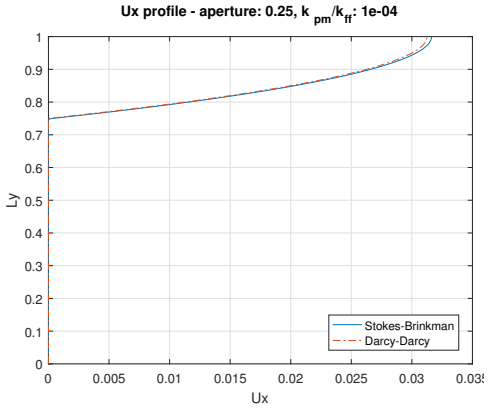

(c) $\gamma = 10^{-4}$

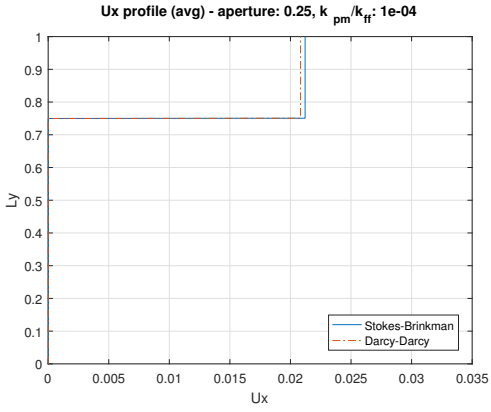

(d) $\gamma = 10^{-4}$

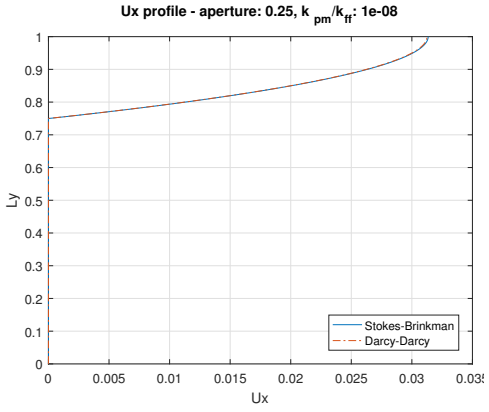

(e) $\gamma = 10^{-8}$

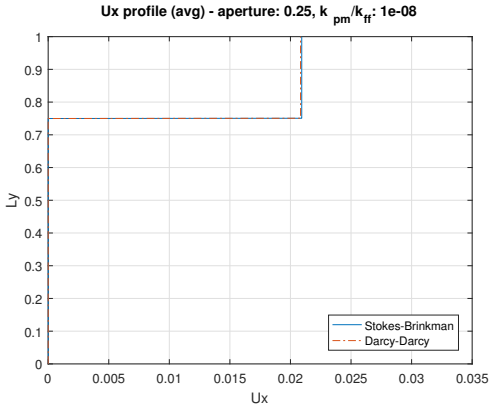

(f) $\gamma = 10^{-8}$

Figure 4.16: Velocity profiles for varying permeability contrasts, $h_f = 1/4$ and $N_{y_f} = 320$

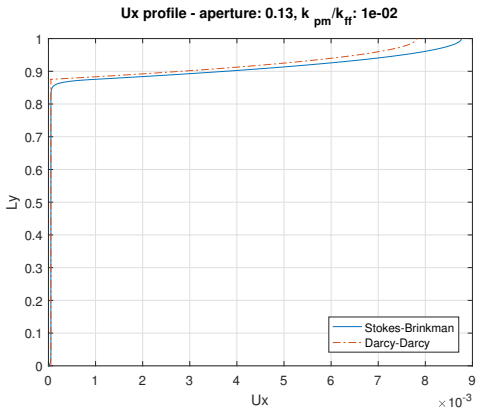

(a) $\gamma = 10^{-2}$

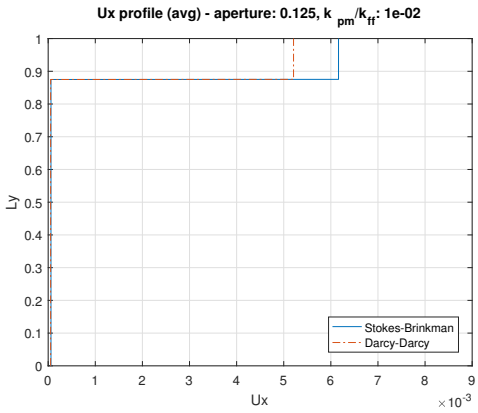

(b) $\gamma = 10^{-2}$

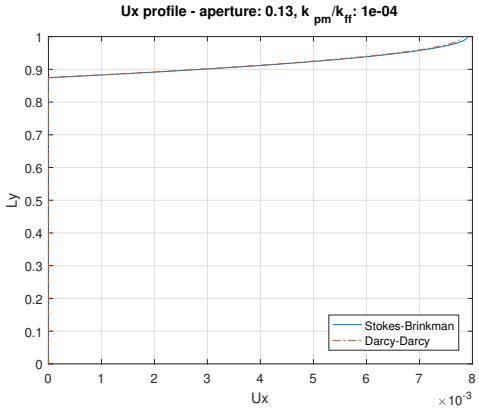

(c) $\gamma = 10^{-4}$

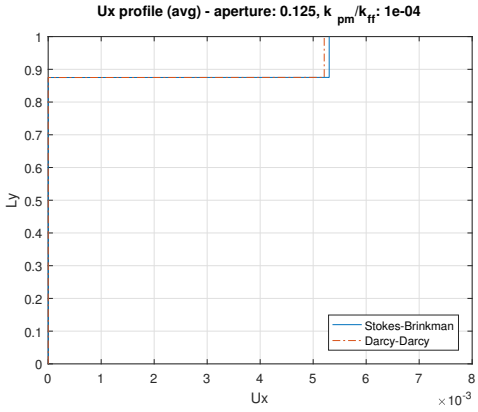

(d) $\gamma = 10^{-4}$

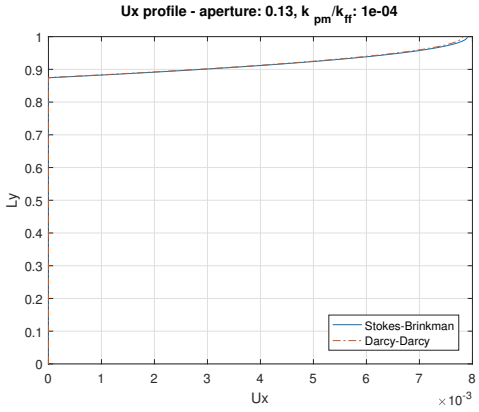

(e) $\gamma = 10^{-8}$

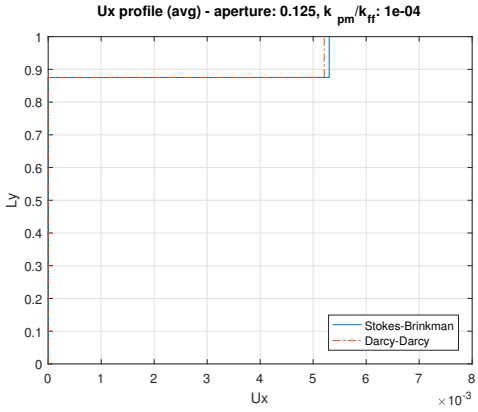

(f) $\gamma = 10^{-8}$

Figure 4.17: Velocity profiles for varying permeability contrasts, $h_f = 1/8$ and $N_{y_f} = 320$

Chapter 5
Conclusion

A threshold of $\gamma = k_{pm}/k_{ff} \approx 10^{-7}$ is revealed from testing sensitivity to porous media permeability, below which the relative error stabilizes, and above which the relative error decreases in the proportion $\epsilon \propto \gamma^{-1/2}$.

The decrease in aperture needs to be followed by an increase in resolution to achieve reasonable results, at a cost of higher computational cost/time. An alternative would be the local refinement of the grid for the areas of the domain where properties and velocity vary substantially more, such as the fracture and the boundary between the two medias, as proposed by the multiscale method.

An insight on which method better suits the application in question is given by the results, which depends on the characteristics of the problem and which particulars are the objects of study.

The Darcy-darcy approach is sufficient for cases of high permeability contrast between porous media and free flow ($\gamma < 10^{-7}$), or simply when the interaction between the two medias is not the focus of study. The Stokes-Brinkman approach is preferred for smaller contrasts between porous media and free flow ($\gamma > 10^{-7}$), i.e., when the porous media is highly permeable.

The fully coupled approach has the advantage of ensuring mass balance and avoids the need of iteration loops, however, for large linear systems, the computational time/cost can be much higher than an iterative method such as the sequential coupling. The elliptic pressure equation used in the latter approach has potential to be exploited in the field of multiscale simulation for more effective simulation, particularly of larger and heterogeneous domains.

Bibliography

Tarek Ahmed et al. *Reservoir engineering handbook*. Gulf Professional Publishing, 2006.

Marco Discacciati and Alfio Quarteroni. Navier-stokes/darcy coupling: modeling, analysis, and numerical approximation. *Revista Matemática Complutense*, 22(2):315–426, 2009. URL `http://eudml.org/doc/43558`.

M Ehrhardt. An introduction to fluid-porous interface coupling. *Progress in computational physics*, 2:3–12, 2000.

Vincenzo Guerriero, Stefano Mazzoli, Alessandro Iannace, Stefano Vitale, Armando Carravetta, and Christoph Strauss. A permeability model for naturally fractured carbonate reservoirs. 40:115–134, 02 2013.

Oleg Iliev and Vsevolod Laptev. On numerical simulation of flow through oil filters. *Computing and Visualization in Science*, 6(2):139–146, Mar 2004. ISSN 1433-0369. doi: 10.1007/s00791-003-0118-8. URL `https://doi.org/10.1007/s00791-003-0118-8`.

Michael Le Bars and M Worster. Interfacial conditions between a pure fluid and a porous medium: Implications for binary alloy solidification. 550:149 – 173, 03 2006.

Quanshu Li, Huilin Xing, Jianjun Liu, and Xiangchon Liu. A review on hydraulic fracturing of unconventional reservoir. *Petroleum*, 1(1):8 – 15, 2015. ISSN 2405-6561. doi: https://doi.org/10.1016/j.petlm.2015.03.008. URL `http://www.sciencedirect.com/science/article/pii/S2405656115000140`.

Gareth McKinley. *2.25 Advanced Fluid Mechanics*. Massachusetts Institute of Technology, 2013. URL `https://ocw.mit.edu`.

Graham Neale and Walter Nader. Practical significance of brinkman's extension of darcy's law: coupled parallel flows within a channel and a bounding porous medium. *The Canadian Journal of Chemical Engineering*, 52(4): 475–478, 1974.

Karsten Pruess. Enhanced geothermal systems (egs) using co2 as working fluid—a novel approach for generating renewable energy with simultaneous sequestration of carbon. *Geothermics*, 35(4):351 – 367, 2006. ISSN 0375-6505. doi: https://doi.org/10.1016/j.geothermics.2006.08.002. URL http://www.sciencedirect.com/science/article/pii/S0375650506000460.

Wook Ryol Hwang and Suresh Advani. Numerical simulations of stokes–brinkman equations for permeability prediction of dual scale fibrous porous media. 22, 11 2010.

S. Sarkar, M.N. Toksoz, and D.R. Burn. Fluid flow modelling in fractures. *MIT Earth Resources Laboratory Industry Consortium Meeting*, 2004.

H.K. Versteeg and W. Malalasekera. *An Introduction to Computational Fluid Dynamics: The Finite Volume Method*. Pearson Education Limited, 2007. ISBN 9780131274983. URL https://books.google.nl/books?id=RvBZ-UMpGzIC.

Robert W. Zimmerman and Gudmundur S. Bodvarsson. Hydraulic conductivity of rock fractures. *Transport in Porous Media*, 23(1):1–30, Apr 1996. ISSN 1573-1634. doi: 10.1007/BF00145263. URL https://doi.org/10.1007/BF00145263.